Timing of Quaternary volcanism and its relationship with tectonics in the central segment of the Ecuadorian Andes

Santiago Santamaria, Xavier Quidelleur, Pablo Samaniego, Laurence Audin, Jean-Luc Le Pennec, Silvana Hidalgo, Herve Guillou, Céline Liorzou

Timing of Quaternary volcanism and its relationship with tectonics in the central segment of the Ecuadorian Andes

Santiago Santamaria [a, b], Xavier Quidelleur [a], Pablo Samaniego [c], Laurence Audin [d], Jean-Luc Le Pennec [c], Silvana Hidalgo [e], Hervé Guillou [f], Céline Liorzou [g]

[a] GEOPS, Université Paris-Saclay, CNRS, Rue du Belvédère, 91405 Orsay, France

[b] Instituto de Investigación Geológico y Energético, De las Malvas E15-142, Quito, Ecuador

[c] Laboratoire Magmas et Volcans, Université Clermont Auvergne, CNRS, IRD, OPGC, F-63000 Clermont-Ferrand, France

[d] Institut des Sciences de la Terre, IRD: UR219, Université Joseph Fourier–Grenoble I–INSU–OSUG, Grenoble, France

[e] Instituto Geofísico, Escuela Politécnica Nacional, Ap. 17-01-2759, Quito, Ecuador

[f] Laboratoire des Sciences du Climat et de l'Environnement, LSCE/IPSL, CEA-CNRS-UVSQ, Université Paris-Saclay, 91190 Gif-sur-Yvette, France

[g] Laboratoire Géosciences Océan, Institut Universitaire Européen de la Mer, Université de Bretagne Occidentale, Rue Dumont d'Urville, 29280 Plouzané, France

Keywords:

- Ecuador
- K-Ar dating
- Quaternary
- Eruptive history
- Tectonics

Highlights:

- Volcanic activity in the central Ecuadorian Andes occurred since at least ~1.3 Ma
- An increase in volcanic activity took place to the south since ~0.6 Ma
- The predominance of older volcanoes to the north suggests an extension of volcanism
- Crustal tectonic structures had a key role in the spatial arrangement of volcanoes
- The overall volcanic output rate has been roughly stable during the last ~0.6 Ma

ABSTRACT

The unusually high number of volcanoes in the Ecuadorian Arc, located in the deformation zone of the continental North Andean Sliver, coincides with the projection of the major oceanic structures observed in the Nazca Plate, such as the Carnegie Ridge and the Grijalva fracture zone. Although the relationship between this tectonic setting and volcanism has been widely discussed in the literature, their temporal relationship has not been thoroughly investigated due to the lack of geochronological data. We present here 20 new K-Ar and 2 $^{40}Ar/^{39}Ar$ ages obtained for 7 volcanoes of the central segment of the Ecuadorian arc, which together with previous data show that volcanism in this area started at ~1.3 Ma. A notable increase in volcanic activity occurred since ~0.6 Ma, when the formation of a dozen volcanoes occurred in a relatively small area of the central segment. While this arrangement of volcanoes, here referred to as a "volcanic cluster", appears to be controlled by crustal tectonic structures, the order of onset of these volcanoes and their eruptive activity does not show clear migration patterns over time. However, the presence of older volcanoes in the north of the central segment suggests a possible southward extension of volcanism between ~1.3 and ~0.6 Ma. Finally, based on the cumulative bulk volumes calculated for the volcanic edifices over time, we infer that the magmatic productivity rate has been roughly constant during the last ~550 kyr in this area.

1. INTRODUCTION

The Northern Andean Volcanic Zone results from the subduction of the oceanic Nazca Plate beneath the northwestern margin of South America (Fig. 1a). In contrast to the narrow array of nearly 40 Quaternary volcanoes in Colombia, more than 80 Quaternary eruptive centers (21 with Holocene activity) form the broad Ecuadorian volcanic arc, which covers an area up to 130 km wide north of 2°S latitude (Hall and Wood, 1985; Pedraza Garcia et al., 2007). Usually, these volcanoes are grouped according to their distribution in along-arc alignments defined by their geographic relationship to the two subparallel mountain ranges that form the Ecuadorian Andes (i.e., the Western and Eastern Cordilleras), the tectonic depression that separates both ranges (i.e., the Inter-Andean Valley), and the sub-Andean Amazonian lowlands (Fig. 1b; e.g., Hall and Beate, 1991; Hall et al., 2008; Ancellin et al., 2017). Moreover, the distribution of volcanoes along the arc is not uniform. In fact, dozens of independent edifices occur in areas of a few square kilometers, with distances between their summits ranging from 6 to 12 km. These "volcanic clusters" alternate along the arc with areas with a small number of volcanoes, which define the three distinct segments of the Ecuadorian arc: northern, central, and southern (Fig., 1c).

Almost all of the Ecuadorian volcanic overlaps the in-land projection of notable subducting structures of the Nazca Plate (Fig. 1a), such as the Grijalva Fracture Zone, and the Carnegie Ridge, the latter created by the motion of the Nazca Plate over the Galápagos hotspot (Meschede and Barckhausen, 2001; Lonsdale, 2005; O'Connor et al., 2007). The presence of these oceanic structures, together with the convex shape of the continental margin, has been interpreted to be responsible for the slab flexure described beneath the Ecuadorian arc (Yepes et al., 2016; Portner et al., 2020). In addition, the oblique convergence of the Nazca Plate is responsible for the motion of the northwestern margin of South America, forming the North Andean Sliver (Witt et al., 2006; Alvarado et al., 2016). This displacement occurs through the Chingual-Cosanga-Pallatanga-Puná (CCPP) fault system (Fig. 1c), which traverses the Ecuadorian Andes and extends northward into Colombia (Witt and Bourgois, 2010; Nocquet et al., 2014; Alvarado et al., 2016). Although several studies have been carried out on the slab structure (e.g., Gutscher et al., 1999; Michaud et al., 2009; Yepes et al., 2016) and the kinematics along crustal faults

(e.g., Fiorini and Tibaldi, 2012; Alvarado et al., 2014, 2016; Baize et al., 2020; Jomard et al., 2021), their relationship with the volcanism is under discussion.

Volcanism in the central segment of the Ecuadorian arc occurs approximately between latitudes 0.1°S and 0.8°S, surrounding Quito, the capital of Ecuador. Twenty kilometers south of Quito, more than a dozen of volcanoes stand in an area 70 km wide (E-W) and 40 km long (N-S) that defines the central volcanic cluster of the Ecuadorian arc (Fig. 1c and 2). Although these volcanoes have been studied individually and on a regional scale for geochemical and stratigraphic purposes (e.g., Chemin, 2004; Hidalgo et al., 2007; Hall and Mothes, 2008; Hall et al., 2017b; Ancellin et al., 2017; Chiaradia et al., 2020; Santamaría et al., 2022), the geochronological data remain scarce and their eruptive histories remain poorly studied (especially for the oldest edifices). In order to investigate the temporal link between volcanism, tectonics and the geodynamic setting, we present here new geochronological data together with new field observations for the volcanoes of the central segment of Ecuador, focusing on its volcanic cluster. By combining the available ages, we describe for the first time the Pleistocene eruptive history of this part of the Ecuadorian arc. Furthermore, this work aims to investigate the relationship between ancient and recent tectonics and the development of volcanism in this area.

2. GEOLOGICAL CONTEXT

2.1. Ecuadorian geological setting

The Ecuadorian continental margin consists of a series of allochthonous and para-autochthonous terrains containing several fault systems and sutures roughly parallel to the trench (Cediel, 2019). The Oriente Foreland Basin (Fig. 1b) corresponds to a sedimentary sequence formed since the Mesozoic that overlies the Precambrian Guyanese craton (Vallejo et al., 2021). The Eastern Cordillera is formed by Paleozoic to Jurassic magmatic and metamorphic belts, whose protholites are of both sedimentary and igneous origin (Litherland et al., 1994; Spikings et al., 2015). The Western Cordillera consists of deformed Cretaceous mafic and ultramafic rocks which are overlain by sequences of marine sediments and volcanic deposits (Vallejo et al., 2019). Further west, the Coastal Forearc

consists of several Mesozoic to Cenozoic sedimentary basins that were formed over an ultramafic basement (Luzieux et al., 2006; Witt et al., 2006; Vallejo et al., 2019). These oceanic terrains are interpreted as the remnants of an oceanic plateau accreted to the continental margin during the Late Cretaceous-Paleogene (Spikings et al., 2010; Vallejo et al., 2019; Jaillard, 2022). The Pujilí suture (Fig. 1c) was formed after this accretionary event. The transition between the terrains of the Western and Eastern Cordilleras is masked by the Inter-Andean Valley, an intramountain basin containing a thick sequence of Miocene-Pliocene volcanoclastic sediments overlying a tectonic *mélange* composed of continental and oceanic units (e.g., Aspden et al., 1995; Hungerbühler et al., 2002; Lavenu et al., 1995; Winkler et al., 2005). The Quaternary volcanic arc overlies the Miocene-Pliocene volcanoclastic deposits found in both Cordilleras and in the Inter-Andean Valley. In particular, the volcanoes of the central segment were built on the sedimentary Silante (Late Oligocene-Middle Miocene) and volcanoclastic Zumbahua (Middle Miocene) formations in the Western Cordillera (Vallejo et al., 2019, 2020), and the Pisayambo volcanics (Miocene) in the Eastern Cordillera (Barberi et al., 1988; Lavenu et al., 1995; Egüez et al., 2017).

2.2. Volcanism in the central volcanic cluster of the Ecuadorian Andes

The central segment of the Ecuadorian volcanic arc occurs roughly between latitudes 0.1°S and 0.8°S (Fig. 1c). Although this distinction primarily includes volcanoes such as Pichincha (Robin et al., 2010), the Chacana caldera (Hall and Mothes, 2008b) and the group of edifices located in the Sub-Andean zone (e.g., Hoffer, 2008; Mothes and Hall, 2008; Salgado et al., 2021), the present study focuses on the volcanic cluster located between the Eastern and Western Cordilleras at 0.4-0.8°S latitudes (Fig. 2). Our study not only includes the volcanoes considered as active, but also those with confirmed or estimated Quaternary activity. The geological background of these volcanoes is summarized below.

The **Almas Santas** volcano (3786 m asl; lat. 0°35'S; long. 78°51'W), located on the western side of the Western Cordillera (Fig. 2), is one of the closest volcanic centers to the trench of the entire Ecuadorian arc (~240 km). This volcano comprises a basal andesitic edifice built during a mostly

effusive stage followed by the emplacement of dacitic to rhyolitic lava domes, such as Cerro Azul, a satellite lava dome located on the eastern flank of Almas Santas. A NW sector collapse partially destroyed the volcanic edifice, probably at the end of its eruptive history (Chemin, 2004; Eissen et al., 2005). No geochronological data are available for Almas Santas; a Middle Pleistocene age has been suggested based on its highly eroded morphology (Chemin, 2004; Eissen et al., 2005).

To the east, four volcanoes are located on the eastern edge of the Western Cordillera, adjacent to the Inter-Andean Valley (Fig. 2). La Carcacha edifice (3880 m asl; lat. 0°19'S; long. 78°36'W) is a volcano dated at ~1.29 Ma (Hidalgo, 2006) associated with the **Atacazo-Ninahuilca volcanic complex**, both located on the southern periphery of Quito. The Atacazo edifice (4455 m asl; lat. 0°21'S; long. 78°37'W), active between ~220 ka and ~83 ka (Hidalgo, 2006), partially covers La Carcacha edifice and experienced a major sector collapse followed by the extrusion of several satellite lava domes around 70 ka (Hidalgo, 2006). At least six Plinian eruptions associated with the Ninahuilca dome complex, formed within the sector collapse amphitheater of the Atacazo edifice, occurred during the Holocene (Hidalgo et al., 2008). To the south, **Corazón** volcano (4784 m asl; lat. 0°32'S; long. 78°40'W) was formed by andesite lava sequences and, like many other volcanic centers in the Western Cordillera, exhibits a prominent sector collapse amphitheater opened to the west (Robles, 2013). A pyramidal peak (glacial horn) created by the intense glacial erosion forms the summit of Corazón above 2800 m asl (Fig. 2b). This structure consists of a thick sequence of monolithical breccias overlain by a sequence of thin lavas. The satellite domes of Cerro Bomboli (with probable Holocene activity; Robles, 2013) and La Moya are located on the northern and eastern flanks of Corazón volcano, respectively. Further south, **Iliniza** volcano (5248 m asl; lat. 0°40'S; long. 78°43'W) is composed of two superimposed stratovolcanoes active between ~124 and ~116 ka, and ~45 and ~25 ka, respectively. Iliniza volcano is surrounded by the Pilongo (~353 ka) and Tishigcuchi (probably Holocene) domes (Hidalgo et al., 2007; Santamaría et al., 2022). The Pongo lava flow (~6 ka) represents its most recent activity (Santamaría et al., 2022).

Three highly eroded volcanoes are located in the Inter-Andean Valley (Fig. 2). East of Corazón, the **Pasochoa** volcano (4199 m asl; lat. 0°28'S; long. 78°29'W) is made up of voluminous basaltic

andesite lava sequences. A groundmass $^{40}Ar/^{39}Ar$ age of 1.33 ± 0.30 Ma was obtained from a southwest lava flow (Opdyke et al., 2006). To the south of Pasochoa, the **Rumiñahui** volcano (4722 m asl; lat. 0°35'S; long. 78°30'W) is formed by two lava sequences that differ in their andesitic composition of mid- to high-potassium, respectively (Starr, 1984). Both volcanoes exhibit eroded collapse amphitheaters on their western flanks. To the southwest, the **Santa Cruz** volcano (3978 m asl; lat. 0°39'S; long. 78°38'W) is composed of andesitic lavas and dacitic domes dated at about 700 ka (Santamaría et al., 2022). Recent data suggest a renewed activity between ~79 and ~60 ka, forming the Loma Saquigua dome (Santamaría et al., 2022). Between the Rumiñahui and Santa Cruz volcanoes stands the *Tiopullo plateau*, a topographic high (3500 m asl.) within the Inter-Andean Valley that divides the Machachi-Guayllabamba basin to the north and the Latacunga basin to the south. The Tiopullo plateau has an elongated NW-SE shape approximately 10 km wide and 5 km long, reaching an elevation of 400 m above the Inter-Andean Valley. The plateau shows flanks slopes of less than 7°, with shallow fluvial incisions, and a flat summit with no significant uplifts. Tiopullo, as well as most of the central segment, is covered by a thick sequence of tephra fall deposits associated with the Cotopaxi volcano (Hall et al., 2017a), making sampling of Tiopullo rocks difficult in this area.

East of Pasochoa, on the western edge on the Eastern Cordillera (Fig. 2), the **Sincholagua** volcano (4873 m asl; lat. 0°32'S; long. 78°22'W) is an eroded edifice for which no geochronological or geochemical data are available. Further south, **Cotopaxi** (5897 m asl; lat. 0°41'S; long. 78°26'W) is the only volcano of this volcanic cluster whose Holocene activity has been thoroughly studied (Cotopaxi II edifice; e.g., Mothes et al., 1998; Hall and Mothes, 2008; Pistolesi et al., 2013; Tsunematsu and Bonadonna, 2015; Vezzoli et al., 2017; Sierra et al., 2019). Its eruptive history began with an ancient rhyolitic volcanic center (Cotopaxi I - Barrancas stage), whose products are preserved on Cotopaxi's present-day southern flank. The remnants of the Cotopaxi-I caldera are overlain by a sequence of andesite lavas and breccias associated with the Morurco Edifice (Cotopaxi I - Morurco stage), located to the south of the ancient caldera rim. A voluminous andesite lava sequence, that flowed ~40 km northward from source through the Pita River valley, is associated with this stage (Hall and Mothes, 2008). The ages of the rhyolite and andesite sequences are not fully constrained. Two fission-track ages

of 0.56 ± 0.04 and 0.54 ± 0.05 Ma were obtained from biotite-rich obsidians by Bigazzi et al. (1997), but unfortunately the sampling sites were not provided. The Cotopaxi-I series and the southern flank of Sincholagua are covered by a thick ignimbrite deposit corresponding to the **Chalupas** caldera-forming eruption that occurred southeast of Cotopaxi (lat. 0°47'S; long. 78°20'W). The Chalupas eruption, dated at 216 ± 5 ka (Bablon et al., 2020b), was followed by the construction of the **Quilindaña** andesite edifice (4876 m asl) dated at ~184 and ~169 ka (Hammersley, 2003; Córdova et al., 2020). Several tephra fall deposits older than 43 ka represent its most recent dated activity (Córdova et al., 2020). **Huañuña** (4197 m asl; lat. 0°37'S; long. 78°14'W) and **Chaupiloma** (also called Rio Valle; 4126 m asl; lat. 0°40'S; long. 78°16'W) are rhyolitic domes located to the north of the Chalupas caldera. Based on stratigraphic evidence, these volcanic centers have been assigned an Holocene age (Mothes and Hall, 2008; Hall et al., 2017b). Northeast of Sincholagua and Huañuña, the **Antisana** volcano (5758 m asl; lat. 0°29'S; long. 78°08'W) consists of three successive andesite edifices constructed since ~400 ka (Hall et al., 2017b), including the voluminous Cuyuja lava sequence dated at 0.21 ± 0.03 Ma (groundmass $^{40}Ar/^{39}Ar$; Opdyke et al., 2006). Stratigraphic evidence suggests that the most recent activity at Antisana may have occurred prior to 800 yr BP (Hall et al., 2017b).

3. METHODS

3.1. Sampling strategy

Field campaigns were conducted between 2016 and 2020 to identify and describe the main volcanic units, to establish their stratigraphic relationships, and to collect fresh rock samples for K-Ar and $^{40}Ar/^{39}Ar$ dating, and whole-rock geochemical analyses. A sledgehammer was used to sample inner parts that were not exposed to ambient air and located away from the outer weathered crust. Due to the scarce information on the stratigraphy of some of the volcanoes in the central cluster, we studied the global structure of each edifice as explained below. In order to cover the maximum number of cone building stages, we sampled, whenever possible, the units located at the summit, mid-altitude, and base

206 of the studied volcanoes. Considering the arrangement of the access routes, our sampling was performed
207 on several flanks of each volcano to ensure an adequate spatial and stratigraphic distribution of the data.

208 At Almas Santas volcano, one sample was recovered from the Tangan columnar jointed lava
209 flow (19EQ36), located in a lower section of its southern flank, near the Río Toachi canyon (Fig. 2a).
210 Based on its stratigraphic position, it corresponds to an early stage of Almas Santas. An additional
211 sample was collected from a metrical andesitic block found at the base of the Cerro Azul satellite cone,
212 on the eastern flank of Almas Santas (19EQ43). A total of thirteen samples were collected from Corazón
213 volcano. Samples 19EQ05, 19EQ07 and 19EQ10 correspond to massive lava flows that form the
214 southern and southwestern summit ridges of the volcano (Fig. 2b). These ridges were probably formed
215 in a late stage of Corazón's history, as they are relatively well preserved from erosion. In addition,
216 sample 19EQ11 was collected from the uppermost section of a lava sequence from the Quitasol river
217 canyon, located at the base of the Bomboli satellite cone (northern foothills of Corazón; Fig. 2a). Further
218 south, a massive lava flow exposed on the northern flank of Corazón was sampled (19EQ13). A juvenile
219 block was collected from a nearby pyroclastic density current (PDC) deposit (19EQ14a). Two samples
220 were taken from a sequence of tephra fall deposits exposed on the northern flank of Corazón (19EQ15a,
221 19EQ15b), probably corresponding to a recent activity at Cerro Bómboli. Finally, an andesitic block
222 was recovered from the monolithological breccias at the base of the pyramidal peak of Corazón
223 (19EQ09), as well as an interlayered lava flow (19EQ08). These breccias are overlain by a thick
224 sequence of thin lava flows (~1-5 m) that form the upper part of the summit. These lavas were sampled
225 at sites 20EQ83 and 20EQ84. Additionally, a dacite block was collected from an avalanche deposit on
226 the northwestern flank (20EQ50) near Atacazo-Ninahuilca volcano.

227 Eight samples were collected at Pasochoa volcano. Four lava flows were sampled from the
228 upper (19EQ31, 19EQ32, 19EQ33) and middle (19EQ34) sections of the radial ridges on the northern
229 flank of the volcano (Fig. 2). Sample 19EQ37 belongs to a lava flow found at the bottom of the Millipaso
230 ravine in the foothills of Pasochoa's southern flank. Samples 19EQ30 and 19EQ38 correspond to two
231 voluminous lava flows observed in the margins of the southeastern and southwestern flanks of the
232 volcano. The scarce exposure of massive lava flows in the summit area precluded sampling; instead,

we collected a sample (19EQ42b) for geochemical analysis from one of the numerous dykes that occur between the uppermost monolithological breccias. Likewise, the summit outcrops of Rumiñahui volcano consist mostly of weathered monolithological breccias and rare massive lava flows intersected by several andesitic dikes, which is suggestive of a highly eroded ancient edifice. An andesitic block was collected from a monolithological breccia exposed near the lower section of the central peak (19EQ35). Samples 19EQ27 and 19EQ39 correspond to massive lava flows observed on the southeastern and northwestern flanks, respectively, whose surface morphology is partially identifiable nowadays. Sample 19EQ28 corresponds to an eroded lava flow observed on the southeast ridge of the volcano, which underlies the 19EQ27 lava flow.

The scarcity of access roads and trails to Sincholagua, together with its eroded morphology and thick cover of Holocene deposits (soils and tephra fall deposits), prevented adequate sampling of this volcano. One sample was collected from a lava flow outcropping on the uppermost section of the southwestern ridge (19EQ41) and another from a distal lava flow located on the northeastern flank (20EQ86). Only sample 19EQ40 belongs to a lava flow from the basal section of the summit area. Following the description of Hall et al. (2008), we collected five samples from the older stages of Cotopaxi volcano. Sample 20EQ77 corresponds to a massive mica-rich obsidian flow (Cotopaxi I - Barrancas stage) outcropping at the base of Morurco peak. Two massive lavas (20EQ76, 20EQ78) were sampled from the overlying sequence composed of andesitic lava flows and monolithological breccias (Cotopaxi I - Morurco stage) outcropping in the upper section of the Morurco river canyon. Finally, two samples of the voluminous lava flow that filled the Pita River valley were collected in the Bocatoma (19EQ29) and Tanipamba (20EQ88) areas.

3.2. K-Ar dating

Twenty unaltered samples from the central volcanic cluster were selected on the basis of meticulous thin-section examinations (Appendix A) for K-Ar dating using the unspiked Cassignol-Gillot technique (Cassignol and Gillot, 1982). This technique has also been applied to date young

volcanic rocks from the Ecuadorian volcanic arc (e.g., Bablon et al., 2018, 2019, 2020a; Santamaría et al., 2022; Samaniego et al., 2022), as well as from other Andean volcanic arc segments (e.g., Germa et al., 2010; Pallares et al., 2016, 2019; Grosse et al., 2018) and worldwide (e.g., Germa et al., 2011; Hildenbrand et al., 2018; Dibacto et al., 2020). All analyses were performed on groundmass, except one on plagioclase phenocrysts (19EQ27) and one on obsidian shards (20EQ77). Samples were manually crushed with a steel mortar and sieved to the 63-80, 80-125, or 125-250 μm fraction sizes, according to their phenocrysts-to-groundmass size ratio. Following a 15 min cleaning in an ultrasonic bath with a 10% HNO_3 solution, they were rinsed with de-ionized water. Magnetic and heavy liquids (bromoform) separation methods were then used to extract the groundmass in a narrow density range, removing phenocrysts potential carriers of excess $^{40}Ar^*$ and any undetected weathered fraction. The Cassignol-Gillot technique was preferentially applied to the groundmass as it is the latest phase assumed to crystallize in equilibrium with the atmosphere, and thus would provide the most probable age of the sample and the emplacement of volcanic deposits.

The Cassignol-Gillot technique is suitable for the detection of minute amounts of radiogenic argon ($^{40}Ar^*$) produced by the radioactive decay of ^{40}K, which may be diluted in ^{40}Ar derived from atmospheric contamination. The difference in the $^{40}Ar/^{39}Ar$ ratios obtained from the sample and from an air aliquot, measured under identical conditions using a 180° sector multi-collector mass spectrometer, allows quantification of the $^{40}Ar^*$ content (%). The detection limit of the mass spectrometer, close to 0.1% for $^{40}Ar^*$ (Quidelleur et al., 2001), allows dating volcanic products even of Holocene age with a relatively small uncertainty (Gillot et al., 2006). The ^{40}Ar signal is regularly calibrated with systematic measurements of the HD-B1 standard with an age of 24.18 ± 0.09 Ma (Schwarz and Trieloff, 2007). The potassium (K) concentration was measured by flame absorption spectroscopy, in conjunction with the standards MDO-G (Gillot et al., 1992) and BCR2 (Raczek et al., 2001) for comparison and correction. Then, the $^{40}K/K$ ratio in nature and the ^{40}K decay constant (Steiger and Jäger, 1977) allow the age of the sample to be calculated. Both potassium and argon measurements were carried out at the GEOPS laboratory (Paris-Saclay University, France) and were performed at least twice to verify their reproducibility within a 1-σ uncertainty range. For a full description of sample

preparation, analytical procedures, and age and uncertainty calculations, the reader is recommended to see Bablon et al. (2018).

3.3. $^{40}Ar/^{39}Ar$ dating

For the sake of comparison with the K-Ar technique, groundmass aliquots of samples 19EQ07 and 20EQ84 from the Corazón volcano were also dated using the $^{40}Ar/^{39}Ar$ technique. This exercise allows us to verify the accuracy of our dating and to highlight the presence or absence of external factors such as alteration and isotopic fractionation that could disturb the K-Ar clock (cf. Schaen et al., 2020). Both samples were irradiated for 60 min in the CLICIT facility of the TRIGA reactor at the Oregon State University. The Alder-Creek Sanidine standard ACs-2 with an age of 1.189 Ma (Niespolo et al., 2017) was used for neutron fluence determination. The complete experimental procedure is described in detail in Guillou et al. (2011). Samples were loaded into a double-vacuum resistance furnace for mid-temperature (~600°C) pre-degassing under pumping, followed by a nine-step incremental heating experiment from approximately 700 to 1200°C. The extracted gases were purified using a Ti sublimation pump and two GP-MK3 SAES Zr-Al getters operating at 400°C. Analyses of the five argon isotopes were performed using a GV5400 instrument. Mass discrimination was calculated from repeated analyses of air pipettes using an $^{40}Ar/^{36}Ar$ ratio of 298.56 (Lee et al., 2006). Interfering isotope corrections, as well as other constants used are reported in Appendix B.

3.4. Whole-rock geochemical analyses

Whole-rock major and trace element contents were measured for all dated samples as well as for the other 15 additional samples collected specifically for geochemical analyses, completing a dataset of 35 new analyses. Agate-crushed powders were analyzed by Inductively Coupled Plasma-Atomic Emission Spectrometry (ICP-AES), at the Geo-Ocean Laboratory, Université de Bretagne Occidental (Brest, France), following the analytical procedure described in Cotten et al. (1995). Relative uncertainties are lower than 1% for SiO_2, and 2% for the other major elements, and 5% for trace

elements. Major element concentrations were recalculated to a total of 100% on a water-free basis and are presented in Appendix C.

3.5. Numerical reconstructions of paleotopographies for volume calculations

Numerical reconstructions of paleotopography provide a useful tool in the comprehension of the size and shape reached by a volcanic edifice while eluding its erosional features (e.g., Grosse et al., 2009, 2020, 2022; Lahitte et al., 2012; Germa et al., 2015; O'Hara and Karlstrom, 2023). Here, we consider the numerical reconstructions as a first approximation of the bulk volume of material accumulated by the volcanic edifice at the end of its construction stage, as well as the amount of material removed since the end of the volcanic activity. For this purpose, we used a 4-m resolution digital elevation model (DEM) developed by the Sigtierras program of the *Ministerio de Agricultura y Ambiente de Ecuador* (www.sigtierras.gob.ec). The structural features were mapped using a slope map obtained from this DEM, as well as field observations, Google Earth® satellite imagery and orthophotography.

Due to the limited stratigraphic constraints of most of the volcanoes studied, we opted for a simple procedure to reconstruct the volcanic edifices. Therefore, we followed the method described by Germa et al. (2015), Bablon et al. (2018, 2020a), and Santamaria et al. (2022), which is summarized as follows. The basal surface of each edifice S_{t0} was modeled using an ordinary kriging interpolation of the ArcGIS® software, which follows the surrounding topography starting from the basal outline of the edifice. We manually draw the basal outline of each volcanic edifice based on available geological maps, slope breaks, curvature maps and satellite imagery. The Kriging interpolation used points of known elevation within 1 km around the basal outline to get a better fit of the modeled S_{t0} surface. A regular 100 m point cloud was extracted from the Sigtierras DEM for each volcanic edifice. Based on previous results from other volcanoes in the region (Bablon et al., 2018, 2020a; Santamaría et al., 2022; Samaniego et al., 2022), we chose a conical model with a circular base and a concave profile shape, interpreted as the surface reached at the end of the construction stage S_{t1}. Such profile corresponds to

the exponential trend line obtained by plotting the elevation of the preserved points against their distance from a vertical symmetry axis. This trend line was shifted to obtain the best fit. Points located in highly eroded areas, such as deep glacial and fluvial valleys, were discarded for profile modeling. Thus, the points preserved in crests or interfluves (*planèzes*) were interpreted as low erosion surfaces. The surface uncertainty at each point $\sigma_{S_{tn}-i}$ is provided by the prediction standard error map resulting from ordinary kriging. The present-day surface topography S_{t2} is interpreted as the result of the erosion of the modeled cone S_{t1} after the quiescence period, including possible large sector collapses, thus maximizing the eroded volume. The construction stage volume v_{cs} and the erosion stage volume v_{es} were calculated by integrating the elevation difference between S_{t0} - S_{t1}, and S_{t1} - S_{t2} surfaces multiplied by the pixel area, respectively. The volume uncertainty σ_v corresponds to the combination of the elevation uncertainties of each point σ_{e-i} multiplied by the pixel area, where $\sigma_{e-i} = \sqrt{{\sigma_{S_{tn}-i}}^2 + {\sigma_{S_{tn+1}-i}}^2}$.

4. RESULTS

4.1. K-Ar dating

Twenty new K-Ar ages are presented in Table 1 and shown in Figure 2. K contents range from 0.76 to 1.75 wt.% for groundmass, reaching a minimum of 0.51 wt.% in plagioclase and a maximum of 2.4 wt.% in obsidian fractions. Radiogenic argon contents range from 0.5% to 28.9%, with a maximum of 47.7% for plagioclase.

Samples from the eastern and southern flanks of Almas Santas volcano yielded similar ages of 374 ± 7 ka (19EQ43) and 364 ± 7 ka (19EQ36), respectively. Considering the sampling bias favoring the upper exposed sections of the edifice, this narrow age range probably represents the youngest cone-building stage of the volcano.

Further east, the Corazón volcano exhibits a wider range of ages between 178 ± 32 and 67 ± 4 ka. Notably, sample 19EQ08, taken from the base of the pyramidal peak was dated at 178 ± 32 ka and

probably represents an older phase of the volcano. A second sample taken slightly higher (Fig. 2b) and dated at 175 ± 30 ka (20EQ84) supports this result. However, we treat both ages with caution due to their high atmospheric contamination and low radiogenic argon content, reflected in their large uncertainty range. An age of 149 ± 6 ka was obtained for a dacite block (20EQ50) collected from a debris avalanche deposit located at the base of the northeastern flank of Corazón volcano. Finally, the ages obtained from the lavas with fresh morphologies at the top of the ridges sampled on the northern and southern flanks define a consistent range between 95 ± 3 ka and 67 ± 4 ka, the latter age being the youngest age obtained for this volcano.

In the Inter-Andean Valley, the five ages obtained for Pasochoa volcano exhibit a narrow range between 472 ± 8 and 423 ± 20 ka (Table 1). This range includes the voluminous lava flow outcropping in the Pita River valley (19EQ30), on the eastern flank of Pasochoa volcano, dated at 450 ± 7 ka. Further south, the highly weathered state of the Rumiñahui volcanic products precluded groundmass analyses. Therefore, we analyzed plagioclase phenocrysts recovered from the less weathered sample 19EQ27, which yielded an age of 207 ± 9 ka. This sample corresponds to a massive porphyritic lava flow from the eastern flank of the volcano, which belongs to the late volcanic stage characterized by high-K lavas (Starr, 1984). Given the possible presence of inherited radiogenic argon in plagioclase crystals (e.g., Singer et al., 1998), this result should be considered as a maximum value for the eruption age.

Similar to Rumiñahui, the Sincholagua lavas show intense weathering in most outcrops. However, a fresh lava sampled on the eastern flank (19EQ41) yielded a groundmass K-Ar age of 316 ± 6 ka. Regarding Cotopaxi-I volcano, the obsidian flow at the base of the Morurco peak yielded an age of 537 ± 11 ka (20EQ77), which is the oldest value obtained in this study. Finally, a lava flow exposed south of Morurco (20EQ78), and the voluminous Pita lava flows (20EQ88) yielded ages of 334 ± 5 ka and 295 ± 10 ka, respectively.

4.2. $^{40}Ar/^{39}Ar$ dating

Plateau ages, isochron regressions and probability of fit were calculated using ArArCalc (Koppers, 2002) following the criteria of Sharp and Renne (2005). An isochron includes the maximum number of consecutive steps with a probability of fit ≥0.1. It consists of at least three or more steps that contain ≥60% of the ^{39}Ar released and it defines a trapped $^{40}Ar/^{36}Ar$ ratio not statistically different from 298.56. Retained criteria for acceptable age plateau are: (1) it must have a minimum of 3 or more consecutive steps that contain 60% or more of the ^{39}Ar released, (2) no resolvable slope at 1σ analytical uncertainty, (3) no outliers or age trends within the initial and final steps.

The step-heating experiments conducted on these two samples allow the calculation of age plateaus with 87.5% (sample 20EQ84) to 97.0% (sample 19EQ07) of total gas released (Fig.3, Appendix B). This is evidence that the K-Ar clock of these samples is not disturbed and that the calculated ages are reliable. Indeed, according to the lost on ignition (LOI) values (-0.09 and 0.64%, Appendix C), both samples are considered unaltered but with a slightly higher value of LOI for sample 20EQ84. This would explain that its apparent age spectrum appears more scattered, with ages ranging from 72 ± 41 to 170 ± 97 ka. Although two consecutive steps (5 and 6) are slightly discordant, we calculated a plateau age of 115.1 ± 15.2 ka for sample 20EQ84. The inverse isochron age of 148.1 ± 48.3 ka appears to be poorly constrained due to the very high atmospheric contamination of this sample, with radiogenic ^{40}Ar content below 3% for all steps. The experiment of sample 19EQ17 yielded a relatively well constrained plateau age of 94.3 ± 4.9 ka and an inverse isochron age of 87.9 ± 11.9 ka. There is no evidence of $^{40}Ar^{*}$ excess or mass fractionation, as the $^{40}Ar/^{36}Ar$ intercept values calculated for the two inverse isochrons (Fig.3) are within uncertainties the current atmospheric value. Therefore, the equivalent but more precise plateau ages will be used in our study.

4.3. Construction and erosion volumes of the central volcanic cluster

The numerical reconstructions allowed us to calculate the bulk volume of the volcanic edifices within the central volcanic cluster, as well as the volume of the material removed by erosion. It should be noted that the surface models used do not take into account the amount of material lost during the construction stages due to erosion or possible sectoral collapses, nor do they take into account far-

reaching products such as tephra fall deposits. Therefore, the edifice volumes obtained here (construction and present-day volumes) are considered as minimum values, while the erosion volumes are considered as maximum solely for their last quiescence period. On the other hand, the heterogeneity of the volcanic materials prevents us from expressing our values as dense rock equivalent (DRE) volumes, and therefore they are reported as bulk volumes. The calculated volumes are presented in Table 2, together with previous volume estimates published for other volcanic centers. Our calculations show that the most voluminous edifice (reconstructed volume) is the Almas Santas volcano with a bulk value of 90 ± 14 km^3, while the smallest is La Carcacha volcano with a value of 8 ± 1 km^3. The average volume reached by the volcanoes of the central volcanic cluster is 43 ± 12 km^3, with Almas Santas being the largest (90 ± 14 km^3) and Carcacha the smallest (8 ± 1 km^3). The present-day volumes of the studied edifices range from 5 ± 1 km^3 (Carcacha volcano) to 44 ± 5 km^3 (Pasochoa volcano), with an average value of 20 km^3. The minimum uncertainty in the volumetric calculations is 10 vol.%, with a maximum of 24 vol.%. The calculated volumes for volcanoes located in areas with irregular relief, such as Almas Santas and Corazón (σ_v > 7 km^3), show larger uncertainties compared to volcanoes located in more regular or better-defined areas, such as Pasochoa or Cotopaxi (σ_v < 6 km^3). Likewise, basement surface roughness in mountain areas may underestimate or overestimate the volumes of volcanoes such as Corazón or Almas Santas, respectively, due to the possible presence of ridges or hills in these regions. The present-day volume of eroded material is of at least 24% of the initial volume. Notably, the Almas Santas, Corazón and Sincholagua volcanoes exhibit the highest erosion percentages, up to 74 vol.% of the pre-erosion volume. Furthermore, the Santa Cruz volcano, partially covered by recent volcanic structures and edifices, presents considerable difficulties in estimating the volume preserved nowadays, thus preventing the calculation of the eroded volume.

Note that output and erosion rates have not been investigated here, given the multiplicity of factors that control these processes, and which are beyond the scope of this research. For instance, factors such as the heterogeneity of the constituent eruptive products in a volcanic edifice, their distribution around the main vent, and their mechanical resistance to erosion could cause noticeable discrepancies in the volume achieved at the end of the construction periods (e.g., Hora et al., 2007;

Zernack et al., 2009; Yamamoto et al., 2018). On the other hand, external factors may influence the rate of syn-eruptive erosion, which in turn biases the output rates. Examples of such factors include the elevation of the edifice and the geographic setting, which influence the precipitation range and/or the extent of glacial cover to which volcanic edifices are exposed through (Brook et al., 2011; Conway et al., 2016; Pure et al., 2020; O'Hara and Karlstrom, 2023). At the same time, tectonic activity can influence both the geometry of the volcanic edifice cone and its degree of degradation (Lagmay et al., 2000; Mathieu et al., 2011; Mathieu and van Wyk de Vries, 2011). Additionally, output and erosion rates are strongly influenced by the degree of knowledge of the eruptive history of each edifice, the dispersion of geochronological information and the uncertainty in radiometric ages (e.g., Bablon et al., 2020a).

4.4. Geochemical characterization

As shown in Figure 4a, most of the samples from this study are classified as medium-K basaltic andesites to dacites, with SiO_2 contents ranging from 53 wt.% to 64 wt.%. The Cotopaxi-I obsidian (20EQ77) is the only rhyolite in the group with 74 wt.% SiO_2. The K_2O contents vary between 0.7 wt.% and 2.7 wt.%. Notably, samples 19EQ37 and 19EQ39, collected from Rumiñahui volcano, lie in the boundary between the medium and high-K calc-alkaline series (Fig. 4a). Our data are consistent with previous studies carried out on the central volcanic cluster. For instance, the sampled lavas from Almas Santas volcano (19EQ36, 19EQ43) fall within the field defined by Chemin (2004) and Eissen et al. (2005). Likewise, the lavas and breccias from the Corazón volcano form a more constrained lower silica andesite field compared to the one provided by Schiano et al. (2010), which is defined by samples collected around Cerro Bómboli. The andesitic lavas of Pasochoa are consistent with the field defined by the same authors. Only two dacite lavas were found in both volcanoes: 19EQ14a and 19EQ33, respectively. The samples collected from Rumiñahui volcano belong to the two sequences described by Starr (1984), with samples 19EQ39 and the dated 19EQ27 belonging to the high-K series. Finally, the Cotopaxi-I samples are consistent with available geochemical data (Bryant et al., 2006; Garrison et al., 2006, 2011). In particular, the obsidian 20EQ77 shows silica and potassium contents similar to those

reported by Bellot-Gurlet et al. (2008), i.e., samples CTX45 and CTX 46 dated by Bigazzi et al. (1997). Considering the analogous mineralogical composition described by these authors, we can argue that our sample corresponds to the same obsidian flow. In addition, samples collected from the Cotopaxi-I southern flank (20EQ76 and 20EQ78) are consistent with the Morurco andesitic series (Garrison et al., 2006). Although the Pita lava flow (19EQ29, 20EQ88) exhibits a lower silica content, plotting close to the field described by the Pasochoa and Rumiñahui lavas, the Cotopaxi-I samples plot along a single trend. Note that the geochemical data available for Cotopaxi-I are scarce, and thus its compositional field is poorly defined.

Overall, the central volcanic cluster exhibits across-arc geochemical variations similar to those described in other areas of the Ecuadorian arc (e.g., Barragan et al., 1998; Bourdon et al., 2003; Hidalgo et al., 2012; Ancellin et al., 2017; Bablon et al., 2019, 2020a). Chondrite-normalized Rare-Earth Elements (REE) plots (Fig. 4b; Sun and McDonough, 1989) show weak fractionation patterns between Light REE (LREE; La, Ce, Nd) and Heavy REE (HREE; Dy, Er, Yb), with no significant Eu anomaly. Trace elements normalized to primitive mantle diagrams (Fig. 4c) show an overall enrichment of Large-Ion Lithophile Elements (LILE; Rb, Ba, and K) and Sr, and depletion of Nb, P, and Ti. The Cotopaxi-I obsidian (20EQ77) has the highest P and Ti negative anomalies. Samples from the volcanoes in the Eastern Cordillera (e.g., Cotopaxi, Sincholagua) exhibit a slight REE enrichment compared to those from the Inter-Andean Valley (e.g., Pasochoa, Rumiñahui), reaching stronger HREE depletions in the Western Cordillera (e.g., Almas Santas, Corazón). Accordingly, most incompatible element contents are higher (e.g., La, Ba, Rb, Sr, Nb) in the Eastern Cordillera volcanoes, i.e., with increasing distance from the trench, while the ratios of fluid-mobile to fluid-immobile (e.g., Ba/Th, Ba/Nb) elements are lower (e.g., Ba/Th vs La; Fig. 5). Variations in REE contents are also observed for each volcano. For instance, the andesite lavas from Almas Santas (19EQ36, 19EQ43) show a slight HREE enrichment compared to the rhyodacite-rhyolite series (Chemin, 2004; Eissen et al., 2005). Likewise, the high-K andesites from Rumiñahui volcano (e.g., 19EQ27, 19EQ39) and the dacite sample 19EQ33 from Pasochoa volcano show the highest LREE enrichments of the Inter-Andean Valley volcanoes. The Pita

River lavas (Cotopaxi I - Morurco stage) are geochemically distinct from the Pasochoa lavas due to their higher contents of incompatible elements and lower fluid-mobile to fluid-immobile ratios (Fig. 5).

Overall, the geochemical evolution of the magmas in the central volcanic cluster is strongly influenced by crustal differentiation processes (cf. recharge, assimilation and fractional crystallization), as suggested by the negative correlation between the compatible elements and the SiO_2 contents (Fig. D1 and D2, Appendix D), as well as by several petrogenetic models proposed for the volcanoes in the area (Barragan et al., 1998; Bourdon et al., 2003; Bryant et al., 2006; Chiaradia et al., 2009; Hidalgo et al., 2012; Ancellin et al., 2017). These models support fractionation of variable amounts of plagioclase, pyroxene, amphibole, and olivine. However, the occurrence of certain lavas with strong Y and HREE depletion reported for volcanoes such as Ilinizas, Almas Santas, and Cotopaxi, can be explained by more complex petrogenetic processes leading to higher amphibole and/or garnet fractionation (cf. Chemin, 2004; Garrison et al., 2006; Hidalgo et al., 2007). Furthermore, the higher fluid-mobile to fluid-immobile ratios observed in volcanoes located closer to the trench (e.g., Almas Santas, Corazón, Pasochoa) suggest a significant role of aqueous slab fluids or melts in the mantle wedge metasomatism (Ancellin et al., 2017). In summary, the geochemical variation of the central volcanic cluster can be explained both by changes in the subducting slab inputs that metasomatize the mantle wedge, and by fractional crystallization, crustal assimilation and magma mixing (e.g., Garrison et al., 2006; Hidalgo et al., 2007, 2012; Chiaradia et al., 2009, 2020; Schiano et al., 2010; Bellver-Baca et al., 2020).

5. DISCUSSION

5.1. Comparison with previous geochronological data

Overall, the new radiometric ages obtained in this study are consistent with others reported in the central volcanic cluster. An unpublished $^{40}Ar/^{39}Ar$ age obtained at the Laboratoire Geoazur (Côte d'Azur University, Nice, France) was obtained for the Corazón volcano (M. Fornari pers. com.). Hand-picked groundmass fragments from the sample BOM-5, collected north of the Bomboli cone (Fig. 2b), yielded a plateau age of 190 ± 10 ka, and a consistent inverse isochron age of 188 ± 10 ka. These values

are significantly older than our K-Ar age of 91 ± 10 ka obtained from a nearby lava flow (19EQ11). Considering the lower stratigraphic position of the BOM-5 sampling site (Fig. 2b; Fig. D3, Appendix D), the occurrence of two lava sequences of different ages is plausible. Indeed, the BOM-5 age falls within the range obtained here for the early cone-building stage of Corazón volcano, dated at 175 ± 30 ka (20EQ84) and 178 ± 32 ka (19EQ08), while the 19EQ11 age is consistent with the late stage, which occurred between 67 ± 4 ka (19EQ05) and 95 ± 3 ka (19EQ07). Nevertheless, the groundmass separation method used in BOM-5 does not prevent the occurrence of phenocrysts or weathered phases, which could have biased the resulting age. Unfortunately, the lack of detailed data, such as age spectrum and isochron age, makes this age difficult to interpret and prevents us from further investigation.

Opdyke et al. (2006) obtained a $^{40}Ar/^{39}Ar$ plateau (three steps only) age of 1.33 ± 0.30 Ma for a normal polarity lava flow (EC-47) sampled on the eastern flank of Pasochoa. The corresponding isochron yielded an age of 1.93 ± 2.88 Ma with an initial $^{40}Ar/^{39}Ar$ ratio of 271 ± 116, indicating high atmospheric contamination. The low precision of this age precludes comparison with the geomagnetic polarity timescale; nevertheless, we note that the geomagnetic field was dominantly reverse during the Matuyama Chron (i.e., 2.58 to 0.77 Ma; Cohen and Gibbard, 2019). Here we provide a K-Ar age of 450 ± 7 ka obtained from a nearby lava flow (19EQ30) belonging to the same unit. Our age is in good agreement not only with the normal polarity reported by Opdyke et al. (2006), but also with our new ages for Pasochoa volcano, which range from 423 ± 10 ka to 472 ± 8 ka (Table 1).

Two obsidian blocks belonging to the Cotopaxi-I rhyolitic stage were previously dated at 540 ± 50 ka (CTX 46) and 560 ± 40 ka (CTX 45) using the obsidian fission-tracks (Bigazzi et al., 1997). By applying the K-Ar method for dating an obsidian flow (20EQ77), we obtained a consistent and well-defined age of 537 ± 11 ka. The geochemical and petrographic similarities observed between our samples and those of Bigazzi et al. (1997), including the presence of biotite and scarce quartz, suggest that we have successfully dated obsidian samples from the same sequence using two different techniques. Note that biotite crystals were removed here during sample preparation process.

5.2. Comparison between K-Ar and $^{40}Ar/^{39}Ar$ ages from this study

Two samples from Corazón volcano were dated here using two techniques, K-Ar and $^{40}Ar/^{39}Ar$, showing contrasting results. This can be explained by the quality of the lava samples and their atmospheric argon contamination. Sample 19EQ07 has a total-gas relatively high radiogenic ^{40}Ar content (3.6-3.9%; Table 1), which allowed precise measurements. In fact, using K-Ar dating, which has a detection limit of 0.1% (Quidelleur et al., 2001), we obtained an age of 95 ± 3 ka. This value is in very good agreement with the $^{40}Ar/^{39}Ar$ plateau age of 94.3 ± 4.9 ka obtained for this sample (Fig. 3). On the other hand, sample 20EQ84 has a low total-gas radiogenic Ar content of only 0.6% (Table1), resulting in a rather poorly constrained K-Ar age of 175 ± 30 ka. This age is compatible at the one-sigma level with the $^{40}Ar/^{39}Ar$ inverse isochron age of 148 ± 48 ka, and at the two-sigma level with the $^{40}Ar/^{39}Ar$ plateau age of 115.1 ± 15.2 ka. This highlights the difficulty of dating groundmass separated from andesitic lavas with high atmosphere contamination using the K-Ar or $^{40}Ar/^{39}Ar$ techniques. Note that the K-Ar age of 178 ± 32 ka obtained for the nearby sample 19EQ08 (Fig. 2b), which is also highly contaminated ($^{40}Ar^*$ lower than 0.6%), is very close to the K-Ar age of 175 ± 30 ka obtained for 20EQ84, and that the four individual analyses for these samples cluster between 175 and 181 ka despite their large uncertainty (Table 1).

This comparison demonstrates that no systematic error has affected either of these dating techniques, and that K-Ar and $^{40}Ar/^{39}Ar$ ages are reliable when obtained for fresh rocks with relatively high radiogenic yields, such as sample 19EQ07.

5.3. Eruptive history of the central segment

Based on our new K-Ar ages, stratigraphic and morphological data, and previous studies carried out in the central segment volcanoes, we present the eruptive history for this area of the Ecuadorian arc as follows (Fig. 6; Table 3).

The oldest eruptive activity appears to have occurred in the north of the central segment. Several geochronological studies suggest that volcanoes such as Pichincha (Robin et al., 2010), Chacana

(Opdyke et al., 2006; Bellot-Gurlet et al., 2008), Cayambe (Samaniego et al., 2005) and Mojanda-Fuya Fuya (Bablon et al., 2020a) were active prior to ~1 Ma. In the central volcanic cluster area, only the Carcacha volcano (Atacazo-Ninahuilca complex; Western Cordillera), adjacent to the Pichincha volcano, has lava flows dated at ~1.30 Ma (Hidalgo, 2006). After a period of apparent quiescence, volcanic activity resumed southward, forming the Santa Cruz volcano in the Inter-Andean Valley at about 702 ± 11 ka (Santamaría et al., 2022). From ~550 ka, the volcanic activity seems to have increased in the central volcanic cluster (Fig. 6). The Cotopaxi-I caldera (Eastern Cordillera) showed large, highly explosive eruptions and effusive activity of rhyolitic affinity dated at 537 ± 11 ka (20EQ77). Later, the construction of the andesitic Pasochoa volcano occurred in the Inter-Andean Valley, which was already active between 472 ± 8 ka (19EQ34) and 423 ± 10 ka (19EQ37). Massive dacite lava flows and PDC deposits, corresponding to the pre-caldera Chalupas volcanic system, erupted in the Eastern Cordillera around 459 ± 9 ka and 418 ± 10 ka (plagioclase $^{40}Ar/^{39}Ar$ plateau ages; Hammersley, 2003).

Eruptive activity throughout the central volcanic cluster occurred between ~400 and ~300 ka. In the Western Cordillera, the onset of the Almas Santas volcano (dated at 374 ± 7 and 364 ± 7 ka) and the extrusion of the Pilongo lava dome (353 ± 6 ka, Iliniza volcano; Santamaría et al., 2022) took place. We also note that the oldest dated activity of the Antisana (from 378 ± 38 ka; Hall et al., 2017b), Cotopaxi-I Morurco (around 334 ± 5 ka), and Sincholagua (around 312 ± 6 ka) volcanoes in the Eastern Cordillera occurred during this period. Due to sampling bias, these ages may mostly correspond to the intermediate or more recent eruptive stages of these volcanoes. We propose that the emplacement of an older edifice of the Rumiñahui volcano occurred during this eruptive stage of the central volcanic cluster, or earlier, as suggested by (1) the widespread exposure of the dyke network in the summit area, which implies a much higher degree of erosion compared to other edifices in the area, and thus a longer-term erosional phase; (2) the upper bound provided by the 207 ± 9 ka age (19EQ27), which belongs to the high-K andesite series defined by Starr (1984); and (3) the required presence of a prominent edifice at the site of Rumiñahui volcano to channel the Pita lava flows (295 ± 10 ka) northward from the Morurco cone (Cotopaxi-I volcano) to its terminus position east of Pasochoa volcano.

599 The apparent quiescence period in the Western Cordillera since ~300 ka ended when the
600 volcanic activity resumed south of Carcacha volcano, forming the basal edifice of Atacazo volcano.
601 This early cone was dated at ~200 ka (groundmass $^{40}Ar/^{39}Ar$ ages; Hidalgo, 2006). Further south, the
602 emplacement of the older Corazón series could have occurred at about 178 ± 32 ka (19EQ08). The
603 block (20EQ50) collected from an avalanche deposit outcropping between Corazón and Atacazo
604 volcanoes yielded a K-Ar age of 149 ± 6 ka. The Sr and Th contents compared to LILE (e.g., Ba) and
605 LREE (e.g., La) of this sample are consistent with those observed at Atacazo volcano (Fig. D4,
606 Appendix D), suggesting that this sample could be associated with Atacazo instead of Corazón. This
607 implies a possible extension of the Atacazo volcanic activity up to ~150 ka, providing an older bound
608 to its southwestern sector collapse.

609 In the Inter-Andean Valley, the activity resumed at Rumiñahui volcano around 207 ± 9 ka
610 (19EQ27), as suggested by the plagioclase K-Ar age obtained from its terminal andesitic series.
611 Nonetheless, since this age could be biased toward too old values by inherited argon (e.g., Singer et al.,
612 2008), it is possible that Rumiñahui volcano was active in more recent times. Synchronously in the
613 Eastern Cordillera, the voluminous Cuyuja lava flow (11 km^3) was erupted from a fissure located to the
614 southeast of Antisana volcano at 210 ± 30 ka (groundmass $^{40}Ar/^{39}Ar$ plateau age; Opdyke et al., 2006;
615 Hall et al., 2017b). Further south, the Chalupas ignimbrite eruption (VEI 7) occurred southeast of
616 Cotopaxi-I volcano at 216 ± 5 ka (Bablon et al., 2020b), forming a ~17 km-wide caldera and a
617 widespread ignimbrite deposit that covered the Inter-Andean Valley (Mothes and Hall, 2008; Bablon
618 et al., 2020b). The early cone-building stages of Quilindaña volcano, an intra-caldera stratovolcano with
619 activity dated at 184 ± 3 ka (Buenavista dome; groundmass $^{40}Ar/^{39}Ar$ age; Córdova et al., 2020; Córdova
620 et al., 2020) and 169 ± 1 ka (plagioclase $^{40}Ar/^{39}Ar$ age; Hammersley, 2003), followed the Chalupas
621 eruption.

622 Finally, the volcanic activity appears to have been restricted to both cordilleras during the last
623 ~100 kyr. In the Western Cordillera, the Atacazo (Hidalgo, 2006) and Corazón volcanoes were active
624 until at least ~70 ka. Simultaneously, the construction of Iliniza volcano occurred to the south of the
625 Pilongo dome, beginning with its northern edifice at ~123-116 ka. It was followed by the onset of its

southern edifice at ~46-25 ka (Santamaría et al., 2022). The growth of the Loma Saquigua cone (79-60 ka) in Santa Cruz volcano is the only eruptive activity documented in the Inter-Andean Valley during this period (Santamaría et al., 2022). Despite the lack of radiometric dates, the stratigraphic and morphological evidence suggests that the Antisana volcano was also active during this interval (Hall et al., 2017b). During the Holocene, the explosive activity of the Ninahuilca dome complex followed the sector collapse of Atacazo volcano (Hidalgo et al., 2008), while the activity of Iliniza volcano was mainly effusive (Santamaría et al., 2022). In the Eastern Cordillera, several explosive rhyolitic eruptions preceded the construction of the andesitic cone of Cotopaxi II (Hall and Mothes, 2008). The fallout stratigraphic relationships observed in the Eastern Cordillera suggest that the activity of the Huañuna and Rio Valle rhyolitic centers apparently occurred during the Holocene (Mothes and Hall, 2008; Hall et al., 2017b), as well as that of Antisana volcano and the Buenavista dome (Quilindaña volcano; Córdova et al., 2020).

5.4. Eruptive volumes

Volumetric calculations indicate that the volcanoes in the central cluster grew to roughly similar sizes (Table 2), reaching average bulk volumes of 43 ± 12 km^3 (reconstructed volume). These volumes provide a first-order estimate of the amount of erupted material, although factors such as the type, distribution and bulk density of the volcanic deposits, as well as their syn-eruptive erosion, are not accounted for. Tephra dispersion outside the volcanic edifice is an additional factor that is not considered in our calculation. For instance, the bulk volume of fallout deposits of the Cotopaxi Holocene (< 4.5 ka) andesitic series is estimated to be between 4 and 9 km^3 (DRE volume ~1.5 to 3.5 km^3; Hall and Mothes, 2008), whereas the calculated bulk volume of the Cotopaxi edifice is 32 ± 3 km^3. We emphasize that all our calculated values should be considered as rough estimates, as more detailed stratigraphic studies are required for each volcano. Figure 7b plots the accumulated bulk-volume of the central volcanic cluster edifices over time. Due to its low density, the bulk volume of the Chalupas ignimbrite of 230 ± 30 km^3 (Bablon et al., 2020b) was replaced by its Dense Rock Equivalent (DRE) of ~100 km^3 (Hall and Mothes, 2008; Crosweller et al., 2012) for comparison purposes only. Figure 7b

653 shows that the cumulative cone-building volume in the central volcanic cluster has been roughly stable
654 at a rate of 1.2 ± 0.2 km^3/kyr ($R^2 = 0.958$) since ~550 ka. Thus, assuming that the cone-building
655 volumes are proportional to the erupted volumes, we suggest that the magmatic production has been
656 relatively constant for the central volcanic cluster during the last ~0.5 Ma. This observation also seems
657 to apply to the clusters located in the northern and southern segments, according to data from Bablon
658 et al. (2019, 2020a) and references therein. Significant variations in growth or magmatic production
659 rates could have occurred throughout the eruptive history of each volcano, and thus, we strongly suggest
660 that this value should be taken with caution due to the calculation assumptions made.

661

662 **5.5. Temporal and spatial arrangement of the central segment volcanoes**

663 The most common volcanic landforms in the central segment are composite stratovolcanoes, lava
664 domes, and calderas which are distributed in NE-SW alignments following the morpho-structural units
665 of the Ecuadorian arc (Fig. 1 and 2). The position of Almas Santas volcano, located 15 km west of the
666 Volcanic Front, makes the central segment one of the widest in the Northern Andes. This location,
667 geographically closer to the trench, is also shared by Quilotoa, a 3 km-wide caldera located 30 km to
668 the south of Almas Santas. Notwithstanding this arrangement, the overall correlation between the
669 temporal evolution and geographic location of these volcanoes is puzzling, especially in the central
670 volcanic cluster. Indeed, Figures 6 and 7a show that although volcanic activity has been continuous in
671 each alignment for the last ~550 ka, it was unevenly distributed. This observation contrasts with the
672 dynamics of the northern and southern segments, for which Bablon et al. (2019, 2020a) described a
673 relative migration to the northwest and south for the same period, respectively. Nevertheless, the
674 occurrence of edifices older than ~1 Ma to the north of the central segment (e.g., Viejo Cayambe,
675 Samaniego et al., 2005; La Carcacha, Hidalgo, 2006; Chacana Caldera, Opdyke et al., 2006; Ruco
676 Pichincha, Robin et al., 2010; Pre-Mojanda lavas, Bablon et al., 2020a) suggests an overall southward
677 extension of Ecuadorian volcanism in this area between roughly 1 Ma and 600 ka (Bablon et al., 2019).
678 From the above considerations, the central segment appears as a key area to better understand the

679 formation of the Ecuadorian arc and the factors that controlled the emplacement of volcanoes in this
680 area.

681 Evidence for the relationship between crustal architecture, and the position and timing of
682 volcanism is still scarce. Nevertheless, we offer a short discussion on this subject with possible issues
683 to be addressed in future research. As highlighted by Litherland and Aspden (1992), the distribution of
684 the Quaternary volcanoes in the Ecuadorian arc seems to be influenced by the major tectonic structures
685 of the continental crust (Fig. 8). In the central volcanic cluster, for instance, the Almas Santas volcano
686 and the Atacazo-Corazón-Iliniza volcanoes occur above ancient NE-SW oriented fault systems that
687 separate the Cretaceous oceanic units of the Western Cordillera (Hughes and Bermúdez, 1997; Hughes
688 and Pilatasig, 2002), e.g., the Pujilí fault. To the east, the tectonic structures of the Eastern Cordillera
689 are covered by thick Neogene volcanic sequences. Nevertheless, the position major structures such as
690 of the Peltetec fault, is inferred in our study area based on the change in slope of the western edge of
691 the Eastern Cordillera. This position coincides with the exposure of the Peltetec fault in the Chota
692 Valley to the north and in the Pisayambo area to the south (Litherland et al., 1994; Winkler et al., 2005).
693 The volcanoes of the Eastern Cordillera form NE-SW alignments that roughly coincide with the
694 orientation and position of these structures. The arrangement of the ancient structures of the Inter-
695 Andean Valley remains unclear due to the scarce basement exposures.

696 Regarding Quaternary tectonics, the central volcanic cluster is located in the interaction zone
697 between the Quito and Latacunga reverse fault systems, which are expressed to the north and south of
698 this area as parallel strands of folds over large major west dipping, blind, en-echelon thrust faults (Fig.
699 9; Fiorini and Tibaldi, 2012; Alvarado et al., 2014, 2016). These structures, which mainly affect the
700 volcano-sedimentary deposits on the eastern margin of the Inter-Andean Valley, seem to converge
701 towards the ancient Pujilí fault at deep (Western Cordillera; Alvarado et al., 2016) beneath the Iliniza
702 and Corazón volcanoes. The relationship of this fault system to volcanism is not clear. Nevertheless, a
703 progressive southward migration of volcanic activity appears to have occurred at the Iliniza volcano,
704 following the NE-SW axis consistent with the projection of the Pujilí suture (Santamaría et al., 2022),
705 while the preserved areas of the western flank of the Corazón volcano show NE-SW faults that possibly

706 contributed to its destabilization and sector collapse. Accordingly, Figure 9 illustrates that shallow
707 seismicity is present in this area of the Western Cordillera along the volcanic and tectonic structures
708 described above. Northeast of Iliniza, the Machachi right-lateral strike-slip fault is hypothesized to run
709 across the Inter-Andean Valley, extending along the NW flank of Rumiñahui volcano toward the SE of
710 Pasochoa volcano (Soulas et al., 1991; Egüez and Yepes, 1994). Although, we found no clear
711 morphological evidence for the Machachi fault trace, its orientation is compatible with the strike-slip
712 focal mechanisms observed south of Iliniza volcano (Pastocalle seismic zone; Basualto and Troncoso,
713 2003) and south of Pasochoa volcano (Pita Valley seismic zone; Hernández et al., 2020). The
714 occurrence of intense historical earthquakes in these zones (Beauval et al., 2010) suggests a potentially
715 higher degree of fault coupling. Furthermore, north of the Cotopaxi volcano, Fiorini and Tibaldi (2012)
716 described several minor strike-slip faults with NNE-SSW orientation in the Pita Valley. For these
717 authors, the Cotopaxi volcano zone acts as a fault transfer zone that accommodates the higher shortening
718 observed in the Latacunga basin compared to the Guayllabamba basin. Therefore, based on these
719 statements, we hypothesize the existence of a NE-SW system of active tectonic structures (albeit
720 blinded) between the Iliniza, Rumiñahui, Pasochoa, and Sincholagua volcanoes, rather than a single
721 failure. We recognize that the identification of active faulting is not straightforward in the central
722 segment due to the continuous cover of this area during the Holocene (mainly by tephra from the
723 Cotopaxi volcano). However, the above evidence suggests that Quaternary tectonics also played a
724 significant role in promoting magma ascent in this area.

725

726 **6. CONCLUSIONS**

727 The 22 new radiometric ages presented in this article provide the first geochronological data
728 for several edifices of the central volcanic cluster of the Ecuadorian Arc. Despite the significant erosion
729 experienced by some edifices, suggesting long-term exposures, most of them were constructed during
730 the Late Pleistocene. The earliest volcanic activity occurred between ~1.3 Ma and ~700 ka with the
731 onset of La Carcacha and Santa Cruz volcanoes (Hidalgo, 2006; Santamaría et al., 2022). From ~550
732 ka onwards, the volcanic activity in the region increased with the gradual formation of a “volcanic

733 cluster" composed of at least a dozen of stratovolcanoes and some smaller volcanic cones and lava
734 domes, spread over an area 70 km wide (E-W) and 40 km long (N-S). These volcanic features seem to
735 have been constructed probably over or near basement-inherited fault systems and sutures. Although
736 several Quaternary NE-SW fault systems have been described in this area (e.g., Soulas et al., 1991;
737 Egüez and Yepes, 1994; Alvarado, 2012; Fiorini and Tibaldi, 2012), the low deformation associated
738 with these systems suggests that they probably played a secondary, albeit important, role in the
739 development of the volcanoes arrangement, however, more research is needed on this topic. Although
740 the spatial development of volcanism in the central segment appears to be random in time, the
741 occurrence of older volcanoes in the north of this area is suggestive of a southward extension of
742 volcanism between ~1 Ma and ~550 ka. Numerical reconstructions show that the volcanic edifices from
743 the central cluster reached typical volumes on the order of 43 ± 12 km^3. Based on the proposed
744 evolutionary history and our volumetric calculations, we infer that the overall volcanic output rate in
745 the region (and presumably the magmatic production rate) has been roughly stable at 1.2 ± 0.2 km^3/kyr
746 during the last ~550 ka. However, we do not exclude the occurrence of sporadic magmatic pulses and
747 short periods of quiescence that could affect this rate over at shorter timescales.

748 **References**

749 Alvarado, A., 2012. Néotectonique et cinématique de la déformation continentale en Equateur (Ph.D.
750 thesis). Université de Grenoble, Grenoble, France.
751 Alvarado, A., Audin, L., Nocquet, J.M., Jaillard, E., Mothes, P., Jarrín, P., Segovia, M., Rolandone,
752 F., Cisneros, D., 2016. Partitioning of oblique convergence in the Northern Andes subduction
753 zone: Migration history and the present-day boundary of the North Andean Sliver in Ecuador.
754 Tectonics 35, 1048–1065. https://doi.org/10.1002/2016TC004117
755 Alvarado, A., Audin, L., Nocquet, J.M., Lagreulet, S., Segovia, M., Font, Y., Lamarque, G., Yepes,
756 H., Mothes, P., Rolandone, F., Jarrín, P., Quidelleur, X., 2014. Active tectonics in Quito,
757 Ecuador, assessed by geomorphological studies, GPS data, and crustal seismicity. Tectonics
758 33, 67–83. https://doi.org/10.1002/2012TC003224
759 Ancellin, M.-A., Samaniego, P., Vlastélic, I., Nauret, F., Gannoun, A., Hidalgo, S., 2017. Across-arc
760 versus along-arc Sr-Nd-Pb isotope variations in the Ecuadorian volcanic arc. Geochemistry,
761 Geophysics, Geosystems 18, 1163–1188. https://doi.org/10.1002/2016GC006679
762 Aspden, J.A., Bonilla, W., Duque, P., 1995. The El Oro metamorphic complex, Ecuador: geology and
763 economic mineral deposits, Overseas geology and mineral resources. British Geological
764 Survey, Keyworth, Nottingham.
765 Bablon, M., Quidelleur, X., Samaniego, P., Le Pennec, J.-L., Audin, L., Jomard, H., Baize, S.,
766 Liorzou, C., Hidalgo, S., Alvarado, A., 2019. Interactions between volcanism and
767 geodynamics in the southern termination of the Ecuadorian arc. Tectonophysics 751, 54–72.
768 https://doi.org/10.1016/j.tecto.2018.12.010
769 Bablon, M., Quidelleur, X., Samaniego, P., Le Pennec, J.-L., Lahitte, P., Liorzou, C., Bustillos, J.E.,
770 Hidalgo, S., 2018. Eruptive chronology of Tungurahua volcano (Ecuador) revisited based on
771 new K-Ar ages and geomorphological reconstructions. Journal of Volcanology and
772 Geothermal Research 357, 378–398. https://doi.org/10.1016/j.jvolgeores.2018.05.007
773 Bablon, M., Quidelleur, X., Samaniego, P., Le Pennec, J.-L., Santamaría, S., Liorzou, C., Hidalgo, S.,
774 Eschbach, B., 2020a. Volcanic history reconstruction in northern Ecuador: insights for
775 eruptive and erosion rates on the whole Ecuadorian arc. Bull Volcanol 82, 11.
776 https://doi.org/10.1007/s00445-019-1346-1
777 Bablon, M., Quidelleur, X., Siani, G., Samaniego, P., Le Pennec, J.-L., Nouet, J., Liorzou, C.,
778 Santamaría, S., Hidalgo, S., 2020b. Glass shard K-Ar dating of the Chalupas caldera major
779 eruption: Main Pleistocene stratigraphic marker of the Ecuadorian volcanic arc. Quaternary
780 Geochronology 57, 101053. https://doi.org/10.1016/j.quageo.2020.101053
781 Baize, S., Audin, L., Alvarado, A., Jomard, H., Bablon, M., Champenois, J., Espin, P., Samaniego, P.,
782 Quidelleur, X., Le Pennec, J.-L., 2020. Active Tectonics and Earthquake Geology Along the

783 Pallatanga Fault, Central Andes of Ecuador. Frontiers in Earth Science 8, 193.
784 https://doi.org/10.3389/feart.2020.00193
785 Barberi, F., Coltelli, M., Ferrara, G., Innocenti, F., Navarro, J.M., Santacroce, R., 1988. Plio-
786 quaternary volcanism in Ecuador. Geological Magazine 125, 1–14.
787 Barragan, R., Geist, D., Hall, M., Larson, P., Mark Kurz, 1998. Subduction controls on the
788 compositions of lavas from the Ecuadorian Andes. Earth and Planetary Science Letters 154,
789 153–166. https://doi.org/10.1016/S0012-821X(97)00141-6
790 Basualto, D., Troncoso, L., 2003. Evidencias de sismicidad en la zona de Pastocalle y una eventual
791 actividad anómala del volcán Cotopaxi. Presented at the 10° Congreso Geológico Chileno,
792 Universidad de Concepción, Concepcion, Chile.
793 Beauval, C., Yepes, H., Bakun, W.H., Egred, J., Alvarado, A., Singaucho, J.-C., 2010. Locations and
794 magnitudes of historical earthquakes in the Sierra of Ecuador (1587–1996). Geophys J Int
795 181, 1613–1633. https://doi.org/10.1111/j.1365-246X.2010.04569.x
796 Bellot-Gurlet, L., Dorighel, O., Poupeau, G., 2008. Obsidian provenance studies in Colombia and
797 Ecuador: obsidian sources revisited. Journal of Archaeological Science 35, 272–289.
798 https://doi.org/10.1016/j.jas.2007.03.008
799 Bellver-Baca, M.T., Chiaradia, M., Beate, B., Beguelin, P., Deriaz, B., Mendez-Chazarra, N.,
800 Villagómez, D., 2020. Geochemical evolution of the Quaternary Chachimbiro Volcanic
801 Complex (frontal volcanic arc of Ecuador). Lithos 356–357, 105237.
802 https://doi.org/10.1016/j.lithos.2019.105237
803 Bernard, B., Andrade, D., 2011. Volcanes Cuaternarios del Ecuador Continental. IGEPN Poster
804 Informativo.
805 Bigazzi, G., Coltelli, M., Halder, J., Osorio, A.M., 1997. Provenance studies of obsidian artefacts
806 using fission track analyses in South America: an overview. Presented at the Congreso
807 Internacional del Americanistas (ICA), Quito, Ecuador, pp. 1–16.
808 Bourdon, E., Eissen, J.-P., Gutscher, M.-A., Monzier, M., Hall, M.L., Cotten, J., 2003. Magmatic
809 response to early aseismic ridge subduction: the Ecuadorian margin case (South America).
810 Earth and Planetary Science Letters 205, 123–138. https://doi.org/10.1016/S0012-
811 821X(02)01024-5
812 Brook, M.S., Neall, V.E., Stewart, R.B., Dykes, R.C., Birks, D.L., 2011. Recognition and
813 paleoclimatic implications of late-Holocene glaciation on Mt Taranaki, North Island, New
814 Zealand. The Holocene 21, 1151–1158. https://doi.org/10.1177/0959683611400468
815 Bryant, J.A., Yogodzinski, G.M., Hall, M.L., Lewicki, J.L., Bailey, D.G., 2006. Geochemical
816 Constraints on the Origin of Volcanic Rocks from the Andean Northern Volcanic Zone,
817 Ecuador. Journal of Petrology 47, 1147–1175. https://doi.org/10.1093/petrology/egl006

Cassignol, C., Gillot, P.-Y., 1982. Range and effectiveness of unspiked potassium-argon dating: experimental groundwork and applications, in: Odin, G.S. (Ed.), Numerical Dating in Stratigraphy. John Wiley & Sons, pp. 159–179.

Cediel, F., 2019. Phanerozoic Orogens of Northwestern South America: Cordilleran-Type Orogens. Taphrogenic Tectonics. The Maracaibo Orogenic Float. The Chocó-Panamá Indenter, in: Cediel, F., Shaw, R.P. (Eds.), Geology and Tectonics of Northwestern South America: The Pacific-Caribbean-Andean Junction, Frontiers in Earth Sciences. Springer International Publishing, Cham, pp. 3–95. https://doi.org/10.1007/978-3-319-76132-9_1

Chemin, S., 2004. Le volcan quaternaire Almas Santas (Cordillère occidentale, Equateur). Etude volcanologique, minéralogique et géochimique (Master's thesis). Université de Lausanne, Lausanne, Suisse.

Chiaradia, M., Müntener, O., Beate, B., 2020. Effects of aseismic ridge subduction on the geochemistry of frontal arc magmas. Earth and Planetary Science Letters 531, 115984. https://doi.org/10.1016/j.epsl.2019.115984

Chiaradia, M., Müntener, O., Beate, B., Fontignie, D., 2009. Adakite-like volcanism of Ecuador: lower crust magmatic evolution and recycling. Contrib Mineral Petrol 158, 563–588. https://doi.org/10.1007/s00410-009-0397-2

Cohen, K.M., Gibbard, P.L., 2019. Global chronostratigraphical correlation table for the last 2.7 million years, version 2019 QI-500. Quaternary International, SI: Quaternary International 500 500, 20–31. https://doi.org/10.1016/j.quaint.2019.03.009

Conway, C.E., Leonard, G.S., Townsend, D.B., Calvert, A.T., Wilson, C.J.N., Gamble, J.A., Eaves, S.R., 2016. A high-resolution 40Ar/39Ar lava chronology and edifice construction history for Ruapehu volcano, New Zealand. Journal of Volcanology and Geothermal Research 327, 152–179. https://doi.org/10.1016/j.jvolgeores.2016.07.006

Córdova, M.D., Mothes, P.A., Gaunt, H.E., Salgado, J., 2020. Post-Caldera Eruptions at Chalupas Caldera, Ecuador: Determining the Timing of Lava Dome Collapse, Hummock Emplacement and Dome Rejuvenation. Front. Earth Sci. 8. https://doi.org/10.3389/feart.2020.548251

Cotten, J., Le Dez, A., Bau, M., Caroff, M., Maury, R.C., Dulski, P., Fourcade, S., Bohn, M., Brousse, R., 1995. Origin of anomalous rare-earth element and yttrium enrichments in subaerially exposed basalts: Evidence from French Polynesia. Chemical Geology 119, 115–138. https://doi.org/10.1016/0009-2541(94)00102-E

Crosweller, H.S., Arora, B., Brown, S.K., Cottrell, E., Deligne, N.I., Guerrero, N.O., Hobbs, L., Kiyosugi, K., Loughlin, S.C., Lowndes, J., Nayembil, M., Siebert, L., Sparks, R.S.J., Takarada, S., Venzke, E., 2012. Global database on large magnitude explosive volcanic eruptions (LaMEVE). J Appl. Volcanol. 1, 4. https://doi.org/10.1186/2191-5040-1-4

DeMets, C., Gordon, R.G., Argus, D.F., 2010. Geologically current plate motions. Geophysical Journal International 181, 1–80. https://doi.org/10.1111/j.1365-246X.2009.04491.x

855 Dibacto, S., Lahitte, P., Karátson, D., Hencz, M., Szakács, A., Biró, T., Kovács, I., Veres, D., 2020.
856 Growth and erosion rates of the East Carpathians volcanoes constrained by numerical models:
857 Tectonic and climatic implications. Geomorphology 368, 107352.
858 https://doi.org/10.1016/j.geomorph.2020.107352
859 Egüez, A., Gaona, M., Albán, A., 2017. Mapa Geológico de la República del Ecuador.
860 Egüez, A., Yepes, H., 1994. Estudio neotectonico y de peligro sismico para el Proyecto Hidroelectrico
861 Toachi. Instituto Ecuatoriano de Electrificacion - INECEL, Quito, Ecuador.
862 Eissen, J.-P., Chemin, S., Bourdon, E., Cotten, J., 2005. Preliminary data on the Almas Santas
863 volcanic center from the Ecuadorian frontal arc, in: ISAG 2005 Extended Abstracts.
864 Presented at the 6th International Symposium on Andean Geodynamics, IRD Éditions,
865 Barcelona, pp. 242–245.
866 Fiorini, E., Tibaldi, A., 2012. Quaternary tectonics in the central Interandean Valley, Ecuador: Fault-
867 propagation folds, transfer faults and the Cotopaxi Volcano. Global and Planetary Change,
868 Coupled deep Earth and surface processes in System Earth: monitoring, reconstruction and
869 process modeling 90–91, 87–103. https://doi.org/10.1016/j.gloplacha.2011.06.002
870 Garrison, J., Davidson, J., Reid, M., Turner, S., 2006. Source versus differentiation controls on U-
871 series disequilibria: Insights from Cotopaxi Volcano, Ecuador. Earth and Planetary Science
872 Letters 244, 548–565. https://doi.org/10.1016/j.epsl.2006.02.013
873 Garrison, J.M., Davidson, J.P., Hall, M., Mothes, P., 2011. Geochemistry and Petrology of the Most
874 Recent Deposits from Cotopaxi Volcano, Northern Volcanic Zone, Ecuador. Journal of
875 Petrology 52, 1641–1678. https://doi.org/10.1093/petrology/egr023
876 Germa, A., Lahitte, P., Quidelleur, X., 2015. Construction and destruction of Mont Pelée volcano:
877 Volumes and rates constrained from a geomorphological model of evolution. Journal of
878 Geophysical Research: Earth Surface 120, 1206–1226. https://doi.org/10.1002/2014JF003355
879 Germa, A., Quidelleur, X., Gillot, P.Y., Tchilinguirian, P., 2010. Volcanic evolution of the back-arc
880 Pleistocene Payun Matru volcanic field (Argentina). Journal of South American Earth
881 Sciences 29, 717–730. https://doi.org/10.1016/j.jsames.2010.01.002
882 Germa, A., Quidelleur, X., Lahitte, P., Labanieh, S., Chauvel, C., 2011. The K–Ar Cassignol–Gillot
883 technique applied to western Martinique lavas: A record of Lesser Antilles arc activity from
884 2Ma to Mount Pelée volcanism. Quaternary Geochronology 6, 341–355.
885 https://doi.org/10.1016/j.quageo.2011.02.001
886 Gillot, P.-Y., Cornette, Y., Max, N., Floris, B., 1992. Two reference materials, Trachytes MDO-G and
887 ISH-G, for Argon Dating (K-Ar and 40Ar/39Ar) of Pleistocene and Holocene rocks.
888 Geostandards Newsletter 16, 55–60. https://doi.org/10.1111/j.1751-908X.1992.tb00487.x
889 Gillot, P.Y., Hildenbrand, A., Lefèvre, J.C., Albore-Livadie, C., 2006. The K/Ar dating method:
890 principle, analytical techniques, and application to Holocene volcanic eruptions in Southern
891 Italy. Acta Vulcanologica 18, 55–66.

892 Grosse, P., Danišík, M., Apaza, F.D., Guzmán, S.R., Lahitte, P., Quidelleur, X., Self, S., Siebe, C.,
893 van Wyk de Vries, B., Ureta, G., Guillong, M., De Rosa, R., Le Roux, P., Wotzlaw, J.-F.,
894 Bachmann, O., 2022. Holocene collapse of Socompa volcano and pre- and post-collapse
895 growth rates constrained by multi-system geochronology. Bull Volcanol 84, 85.
896 https://doi.org/10.1007/s00445-022-01594-0
897 Grosse, P., Ochi Ramacciotti, M.L., Escalante Fochi, F., Guzmán, S., Orihashi, Y., Sumino, H., 2020.
898 Geomorphology, morphometry, spatial distribution and ages of mafic monogenetic volcanoes
899 of the Peinado and Incahuasi fields, southernmost Central Volcanic Zone of the Andes.
900 Journal of Volcanology and Geothermal Research 401, 106966.
901 https://doi.org/10.1016/j.jvolgeores.2020.106966
902 Grosse, P., Orihashi, Y., Guzmán, S.R., Sumino, H., Nagao, K., 2018. Eruptive history of Incahuasi,
903 Falso Azufre and El Cóndor Quaternary composite volcanoes, southern Central Andes. Bull
904 Volcanol 80, 1–26. https://doi.org/10.1007/s00445-018-1221-5
905 Grosse, P., Vries, B. van W. de, Petrinovic, I.A., Euillades, P.A., Alvarado, G.E., 2009. Morphometry
906 and evolution of arc volcanoes. Geology 37, 651–654. https://doi.org/10.1130/G25734A.1
907 Guillou, H., Nomade, S., Carracedo, J.C., Kissel, C., Laj, C., Perez Torrado, F.J., Wandres, C., 2011.
908 Effectiveness of combined unspiked K–Ar and 40Ar/39Ar dating methods in the 14C age
909 range. Quaternary Geochronology 6, 530–538. https://doi.org/10.1016/j.quageo.2011.03.011
910 Gutscher, M.-A., Malavieille, J., Lallemand, S., Collot, J.-Y., 1999. Tectonic segmentation of the
911 North Andean margin: impact of the Carnegie Ridge collision. Earth and Planetary Science
912 Letters 168, 255–270. https://doi.org/10.1016/S0012-821X(99)00060-6
913 Hall, M.L., Beate, B., 1991. El volcanismo plio cuaternario en los Andes del Ecuador, in: El paisaje
914 volcánico de la sierra ecuatoriana: geomorfología, fenómenos volcánicos y recursos
915 asociados, Estudios de Geografia. Corporación Editora Nacional, Quito, pp. 5–17.
916 Hall, M.L., Mothes, P., 2008. The rhyolitic–andesitic eruptive history of Cotopaxi volcano, Ecuador.
917 Bull Volcanol 70, 675–702. https://doi.org/10.1007/s00445-007-0161-2
918 Hall, M.L., Mothes, P., Vallance, J., Alvarado, A., 2017a. Deslizamientos del Yacupungo, in: Cabero,
919 A., Zúñiga, M.A., Le Pennec, J.-L., Narváez, D., Hernández, M.J., Nocquet, J.M., Gómez,
920 F.V. (Eds.), Memorias VIII Jornadas En Ciencias de La Tierra. Presented at the VIII Jornadas
921 en Ciencas de la Tierra, EPN Editorial, Quito, Ecuador, pp. 85–87.
922 Hall, M.L., Mothes, P.A., Samaniego, P., Militzer, A., Beate, B., Ramón, P., Robin, C., 2017b.
923 Antisana volcano: A representative andesitic volcano of the eastern cordillera of Ecuador:
924 Petrography, chemistry, tephra and glacial stratigraphy. Journal of South American Earth
925 Sciences 73, 50–64. https://doi.org/10.1016/j.jsames.2016.11.005
926 Hall, M.L., Samaniego, P., Le Pennec, J.L., Johnson, J.B., 2008. Ecuadorian Andes volcanism: A
927 review of Late Pliocene to present activity. Journal of Volcanology and Geothermal Research,

928 Recent and active volcanism in the Ecuadorian Andes 176, 1–6.
929 https://doi.org/10.1016/j.jvolgeores.2008.06.012
930 Hall, M.L., Wood, C.A., 1985. Volcano-tectonic segmentation of the northern Andes. Geology 13,
931 203–207. https://doi.org/10.1130/0091-7613(1985)13<203:VSOTNA>2.0.CO;2
932 Hammersley, L.C., 2003. Isotopic evidence for the relative roles of fractional crystallization, crustal
933 assimilation and magma supply in the generation of large volume rhyolitic eruptions (Ph.D.
934 thesis). University of California, Berkeley, CA.
935 Hernández, S., Acosta, E., Barros, J., Acero, W., 2020. Sismos en Ecuador - Pichincha (Informe
936 Sísmico Especial No. 2020– 009). Instituto Geofísico, Escuela Politécnica Nacional, Quito,
937 Ecuador.
938 Hidalgo, S., 2006. Les intéractions entre magmas calco-alcalins “classiques” et adakitiques: exemple
939 du complexe volcanique Atacazo-Ninahuilca (Equateur) (Ph.D. thesis). Université Blaise
940 Pascal - Clermont-Ferrand II, Clermont-Ferrand, France.
941 Hidalgo, S., Gerbe, M.C., Martin, H., Samaniego, P., Bourdon, E., 2012. Role of crustal and slab
942 components in the Northern Volcanic Zone of the Andes (Ecuador) constrained by Sr–Nd–O
943 isotopes. Lithos 132–133, 180–192. https://doi.org/10.1016/j.lithos.2011.11.019
944 Hidalgo, S., Monzier, M., Almeida, E., Chazot, G., Eissen, J.-P., van der Plicht, J., Hall, M.L., 2008.
945 Late Pleistocene and Holocene activity of the Atacazo–Ninahuilca Volcanic Complex
946 (Ecuador). Journal of Volcanology and Geothermal Research, Recent and active volcanism in
947 the Ecuadorian Andes 176, 16–26. https://doi.org/10.1016/j.jvolgeores.2008.05.017
948 Hidalgo, S., Monzier, M., Martin, H., Chazot, G., Eissen, J.-P., Cotten, J., 2007. Adakitic magmas in
949 the Ecuadorian Volcanic Front: Petrogenesis of the Iliniza Volcanic Complex (Ecuador).
950 Journal of Volcanology and Geothermal Research 159, 366–392.
951 https://doi.org/10.1016/j.jvolgeores.2006.07.007
952 Hildenbrand, A., Marques, F.O., Catalão, J., 2018. Large-scale mass wasting on small volcanic
953 islands revealed by the study of Flores Island (Azores). Scientific Reports 8, 13898.
954 https://doi.org/10.1038/s41598-018-32253-0
955 Hoffer, G., 2008. Fusion partielle d’un manteau métasomatisé par un liquide adakitique : approches
956 géochimique et expérimentale de la genèse et de l’évolution des magmas de l’arrière-arc
957 équatorien (Ph.D. thesis). Université Blaise Pascal - Clermont-Ferrand II, Clermont-Ferrand,
958 France.
959 Hora, J.M., Singer, B.S., Wörner, G., 2007. Volcano evolution and eruptive flux on the thick crust of
960 the Andean Central Volcanic Zone: 40Ar/39Ar constraints from Volcán Parinacota, Chile.
961 GSA Bulletin 119, 343–362. https://doi.org/10.1130/B25954.1
962 Hughes, R.A., Bermúdez, R., 1997. Geology of the Cordillera Occidental of Ecuador between 0°00’
963 and 1°00’S (No. 4), Proyecto de Desarrollo Minero y Control Ambiental. Cogidem - Brithis
964 Geological Survey, Quito.

965 Hughes, R.A., Pilatasig, L.F., 2002. Cretaceous and Tertiary terrane accretion in the Cordillera
966 Occidental of the Andes of Ecuador. Tectonophysics, Andean Geodynamics ISAG 4 345, 29–
967 48. https://doi.org/10.1016/S0040-1951(01)00205-0
968 Hungerbühler, D., Steinmann, M., Winkler, W., Seward, D., Egüez, A., Peterson, D.E., Helg, U.,
969 Hammer, C., 2002. Neogene stratigraphy and Andean geodynamics of southern Ecuador.
970 Earth-Science Reviews 57, 75–124. https://doi.org/10.1016/S0012-8252(01)00071-X
971 Jaillard, E., 2022. Late Cretaceous-Paleogene orogenic build-up of the Ecuadorian Andes: Review
972 and discussion. Earth-Science Reviews 230, 104033.
973 https://doi.org/10.1016/j.earscirev.2022.104033
974 Jomard, H., Saqui, D., Baize, S., Alvarado, A., Bernard, B., Audin, L., Hidalgo, S., Pacheco, D., Ruiz,
975 M., Segovia, M., 2021. Interactions between active tectonics and gravitational deformation
976 along the Billecocha fault system (Northern Ecuador): Insights from morphological and
977 paleoseismological investigations. Journal of South American Earth Sciences 111, 103406.
978 https://doi.org/10.1016/j.jsames.2021.103406
979 Lagmay, A.M.F., van Wyk de Vries, B., Kerle, N., Pyle, D.M., 2000. Volcano instability induced by
980 strike-slip faulting. Bull Volcanol 62, 331–346. https://doi.org/10.1007/s004450000103
981 Lahitte, P., Samper, A., Quidelleur, X., 2012. DEM-based reconstruction of southern Basse-Terre
982 volcanoes (Guadeloupe archipelago, FWI): Contribution to the Lesser Antilles Arc
983 construction rates and magma production. Geomorphology, Volcano Geomorphology:
984 landforms, processes and hazards 136, 148–164.
985 https://doi.org/10.1016/j.geomorph.2011.04.008
986 Lavenu, A., Winter, T., Dávila, F., 1995. A Pliocene–Quaternary compressional basin in the
987 Interandean Depression, Central Ecuador. Geophysical Journal International 121, 279–300.
988 https://doi.org/10.1111/j.1365-246X.1995.tb03527.x
989 Lee, J.-Y., Marti, K., Severinghaus, J.P., Kawamura, K., Yoo, H.-S., Lee, J.B., Kim, J.S., 2006. A
990 redetermination of the isotopic abundances of atmospheric Ar. Geochimica et Cosmochimica
991 Acta 70, 4507–4512. https://doi.org/10.1016/j.gca.2006.06.1563
992 Litherland, M., Aspden, J.A., 1992. Terrane-boundary reactivation: A control on the evolution of the
993 Northern Andes. Journal of South American Earth Sciences 5, 71–76.
994 https://doi.org/10.1016/0895-9811(92)90060-C
995 Litherland, M., Aspden, J.A., Jemielita, R.A., 1994. The metamorphic belts of Ecuador, Overseas
996 Memoir Institute of Geological Sciences. British Geological Survey, Keyworth, Nottingham.
997 Lonsdale, P., 2005. Creation of the Cocos and Nazca plates by fission of the Farallon plate.
998 Tectonophysics 404, 237–264. https://doi.org/10.1016/j.tecto.2005.05.011
999 Luzieux, L.D.A., Heller, F., Spikings, R., Vallejo, C.F., Winkler, W., 2006. Origin and Cretaceous
1000 tectonic history of the coastal Ecuadorian forearc between 1°N and 3°S: Paleomagnetic,

radiometric and fossil evidence. Earth and Planetary Science Letters 249, 400–414. https://doi.org/10.1016/j.epsl.2006.07.008

Mathieu, L., van Wyk de Vries, B., 2011. The impact of strike-slip, transtensional and transpressional fault zones on volcanoes. Part 1: Scaled experiments. Journal of Structural Geology 33, 907–917. https://doi.org/10.1016/j.jsg.2011.03.002

Mathieu, L., van Wyk de Vries, B., Pilato, M., Troll, V.R., 2011. The interaction between volcanoes and strike-slip, transtensional and transpressional fault zones: Analogue models and natural examples. Journal of Structural Geology 33, 898–906. https://doi.org/10.1016/j.jsg.2011.03.003

Meschede, M., Barckhausen, U., 2001. The relationship of the Cocos and Carnegie ridges: age constraints from paleogeographic reconstructions. Int J Earth Sci 90, 386–392. https://doi.org/10.1007/s005310000155

Michaud, F., Witt, C., Royer, J.-Y., 2009. Influence of the subduction of the Carnegie volcanic ridge on Ecuadorian geology: Reality and fiction, in: Ramos, V.A., Dickinson, W.R., Kay, S.M. (Eds.), Backbone of the Americas: Shallow Subduction, Plateau Uplift, and Ridge and Terrane Collision, Memoir - Geological Society of America. The Geological Society of America, pp. 217–228. https://doi.org/10.1130/2009.1204(10)

Mothes, P.A., Hall, M.L., 2008. Rhyolitic calderas and centers clustered within the active andesitic belt of Ecuador's Eastern Cordillera, in: Volume 3: Collapse Calderas Workshop. Presented at the IOP Conference Series: Earth and Environmental Science, IOP Publishing, Querétaro, Mexico, p. 012007. https://doi.org/10.1088/1755-1307/3/1/012007

Mothes, P.A., Hall, M.L., Janda, R.J., 1998. The enormous Chillos Valley Lahar: an ash-flow-generated debris flow from Cotopaxi Volcano, Ecuador. Bull Volcanol 59, 233–244. https://doi.org/10.1007/s004450050188

Niespolo, E.M., Rutte, D., Deino, A.L., Renne, P.R., 2017. Intercalibration and age of the Alder Creek sanidine 40Ar/39Ar standard. Quaternary Geochronology 39, 205–213. https://doi.org/10.1016/j.quageo.2016.09.004

Nocquet, J.-M., Villegas-Lanza, J.C., Chlieh, M., Mothes, P.A., Rolandone, F., Jarrin, P., Cisneros, D., Alvarado, A., Audin, L., Bondoux, F., Martin, X., Font, Y., Régnier, M., Vallée, M., Tran, T., Beauval, C., Mendoza, J.M.M., Martinez, W., Tavera, H., Yepes, H., 2014. Motion of continental slivers and creeping subduction in the northern Andes. Nature Geoscience 7, 287–291. https://doi.org/10.1038/ngeo2099

O'Connor, J.M., Stoffers, P., Wijbrans, Jan.R., Worthington, T.J., 2007. Migration of widespread long-lived volcanism across the Galápagos Volcanic Province: Evidence for a broad hotspot melting anomaly? Earth and Planetary Science Letters 263, 339–354. https://doi.org/10.1016/j.epsl.2007.09.007

O'Hara, D., Karlstrom, L., 2023. The arc-scale spatial distribution of volcano erosion implies coupled magmatism and regional climate in the Cascades arc, United States. Frontiers in Earth Science 11.

Opdyke, N.D., Hall, M., Mejia, V., Huang, K., Foster, D.A., 2006. Time-averaged field at the equator: Results from Ecuador. Geochemistry, Geophysics, Geosystems 7. https://doi.org/10.1029/2005GC001221

Pallares, C., Quidelleur, X., Debreil, J.A., Antoine, C., Sarda, P., Tchilinguirian, P., Delpech, G., Gillot, P.-Y., 2019. Quaternary evolution of the El Tromen volcanic system, Argentina, based on new K-Ar and geochemical data: Insights for temporal evolution of magmatic processes between arc and back-arc settings. Journal of South American Earth Sciences 90, 338–354. https://doi.org/10.1016/j.jsames.2018.12.022

Pallares, C., Quidelleur, X., Gillot, P.-Y., Kluska, J.-M., Tchilinguirian, P., Sarda, P., 2016. The temporal evolution of back-arc magmas from the Auca Mahuida shield volcano (Payenia Volcanic Province, Argentina). Journal of Volcanology and Geothermal Research 323, 19–37. https://doi.org/10.1016/j.jvolgeores.2016.04.043

Peccerillo, A., Taylor, S.R., 1976. Geochemistry of eocene calc-alkaline volcanic rocks from the Kastamonu area, Northern Turkey. Contr. Mineral. and Petrol. 58, 63–81. https://doi.org/10.1007/BF00384745

Pedraza Garcia, P., Vargas, C.A., Monsalve J., H., 2007. Geometric model of the Nazca plate subduction in southwest Colombia. Earth Sciences Research Journal 11, 124–134.

Pistolesi, M., Cioni, R., Rosi, M., Cashman, K.V., Rossotti, A., Aguilera, E., 2013. Evidence for lahar-triggering mechanisms in complex stratigraphic sequences: the post-twelfth century eruptive activity of Cotopaxi Volcano, Ecuador. Bull Volcanol 75, 1–18. https://doi.org/10.1007/s00445-013-0698-1

Portner, D.E., Rodríguez, E.E., Beck, S., Zandt, G., Scire, A., Rocha, M.P., Bianchi, M.B., Ruiz, M., França, G.S., Condori, C., Alvarado, P., 2020. Detailed Structure of the Subducted Nazca Slab into the Lower Mantle Derived From Continent-Scale Teleseismic P Wave Tomography. Journal of Geophysical Research: Solid Earth 125, e2019JB017884. https://doi.org/10.1029/2019JB017884

Pure, L.R., Leonard, G.S., Townsend, D.B., Wilson, C.J.N., Calvert, A.T., Cole, R.P., Conway, C.E., Gamble, J.A., Smith, T. 'Bubs,' 2020. A high resolution 40Ar/39Ar lava chronology and edifice construction history for Tongariro volcano, New Zealand. Journal of Volcanology and Geothermal Research 403, 106993. https://doi.org/10.1016/j.jvolgeores.2020.106993

Quidelleur, X., Gillot, P.-Y., Soler, V., Lefèvre, J.-C., 2001. K/Ar dating extended into the last millennium: Application to the youngest effusive episode of the Teide Volcano (Spain). Geophysical Research Letters 28, 3067–3070. https://doi.org/10.1029/2000GL012821

Raczek, I., Stoll, B., Hofmann, A.W., Peter Jochum, K., 2001. High-Precision Trace Element Data for the USGS Reference Materials BCR-1, BCR-2, BHVO-1, BHVO-2, AGV-1, AGV-2, DTS-1, DTS-2, GSP-1 and GSP-2 by ID-TIMS and MIC-SSMS. Geostandards Newsletter 25, 77–86. https://doi.org/10.1111/j.1751-908X.2001.tb00789.x

Robin, C., Samaniego, P., Le Pennec, J.-L., Fornari, M., Mothes, P., van der Plicht, J., 2010. New radiometric and petrological constraints on the evolution of the Pichincha volcanic complex (Ecuador). Bull Volcanol 72, 1109–1129. https://doi.org/10.1007/s00445-010-0389-0

Robles, A., 2013. Estudio de depósitos volcánicos del Cuaternario en la zona sur del Distrito Metropolitano de Quito (Engineer memoir). Escuela Politécnica Nacional, Quito, Ecuador.

Salgado, J.A., Mothes, P.A., Córdova, M.D., 2021. New observations on the recent eruptive activity of Sumaco Volcano (Ecuador), based on geochronology, stratigraphy and petrography. Journal of South American Earth Sciences 112, 103568. https://doi.org/10.1016/j.jsames.2021.103568

Samaniego, P., Martin, H., Monzier, M., Robin, C., Fornari, M., Eissen, J.-P., Cotten, J., 2005. Temporal Evolution of Magmatism in the Northern Volcanic Zone of the Andes: The Geology and Petrology of Cayambe Volcanic Complex (Ecuador). Journal of Petrology 46, 2225–2252. https://doi.org/10.1093/petrology/egi053

Samaniego, P., Ordóñez, J., Bablon, M., Hall, M.L., Quidelleur, X., Lahitte, P., Santamaria, S., Liorzou, C., 2022. The eruptive chronology of the Carihuairazo volcano (Ecuador): Recurrent sector collapses of a Middle Pleistocene stratovolcano of the northern andes. Journal of South American Earth Sciences 116, 103865. https://doi.org/10.1016/j.jsames.2022.103865

Santamaría, S., Quidelleur, X., Hidalgo, S., Samaniego, P., Le Pennec, J.-L., Liorzou, C., Lahitte, P., Córdova, M., Espín, P., 2022. Geochronological evolution of the potentially active Iliniza Volcano (Ecuador) based on new K-Ar ages. Journal of Volcanology and Geothermal Research 424, 107489. https://doi.org/10.1016/j.jvolgeores.2022.107489

Schaen, A.J., Jicha, B.R., Hodges, K.V., Vermeesch, P., Stelten, M.E., Mercer, C.M., Phillips, D., Rivera, T.A., Jourdan, F., Matchan, E.L., Hemming, S.R., Morgan, L.E., Kelley, S.P., Cassata, W.S., Heizler, M.T., Vasconcelos, P.M., Benowitz, J.A., Koppers, A.A.P., Mark, D.F., Niespolo, E.M., Sprain, C.J., Hames, W.E., Kuiper, K.F., Turrin, B.D., Renne, P.R., Ross, J., Nomade, S., Guillou, H., Webb, L.E., Cohen, B.A., Calvert, A.T., Joyce, N., Ganerød, M., Wijbrans, J., Ishizuka, O., He, H., Ramirez, A., Pfänder, J.A., Lopez-Martínez, M., Qiu, H., Singer, B.S., 2020. Interpreting and reporting 40Ar/39Ar geochronologic data. GSA Bulletin 133, 461–487. https://doi.org/10.1130/B35560.1

Schiano, P., Monzier, M., Eissen, J.-P., Martin, H., Koga, K.T., 2010. Simple mixing as the major control of the evolution of volcanic suites in the Ecuadorian Andes. Contrib Mineral Petrol 160, 297–312. https://doi.org/10.1007/s00410-009-0478-2

1109 Schwarz, W.H., Trieloff, M., 2007. Intercalibration of 40Ar–39Ar age standards NL-25, HB3gr
1110 hornblende, GA1550, SB-3, HD-B1 biotite and BMus/2 muscovite. Chemical Geology 242,
1111 218–231. https://doi.org/10.1016/j.chemgeo.2007.03.016
1112 Sierra, D., Vasconez, F., Andrade, S.D., Almeida, M., Mothes, P., 2019. Historical Distal Lahar
1113 Deposits on the Remote Eastern-Drainage of Cotopaxi Volcano, Ecuador. Journal of South
1114 American Earth Sciences 95, 102251. https://doi.org/10.1016/j.jsames.2019.102251
1115 Singer, B.S., Jicha, B.R., Harper, M.A., Naranjo, J.A., Lara, L.E., Moreno-Roa, H., 2008. Eruptive
1116 history, geochronology, and magmatic evolution of the Puyehue-Cordón Caulle volcanic
1117 complex, Chile. GSA Bulletin 120, 599–618. https://doi.org/10.1130/B26276.1
1118 Soulas, J.-P., Eguez, A., Yepes, Hugo, Perez, H., 1991. Tectónica activa y riesgo sísmico en los
1119 Andes Ecuatorianos y el extremo sur de Colombia. Bol. Geol. Ecuat. 2, 3–11.
1120 Spikings, R., Cochrane, R., Villagomez, D., Van der Lelij, R., Vallejo, C., Winkler, W., Beate, B.,
1121 2015. The geological history of northwestern South America: from Pangaea to the early
1122 collision of the Caribbean Large Igneous Province (290–75Ma). Gondwana Research 27, 95–
1123 139. https://doi.org/10.1016/j.gr.2014.06.004
1124 Spikings, R., Crowhurst, P.V., Winkler, W., Villagomez, D., 2010. Syn- and post-accretionary
1125 cooling history of the Ecuadorian Andes constrained by their in-situ and detrital
1126 thermochronometric record. Journal of South American Earth Sciences 30, 121–133.
1127 https://doi.org/10.1016/j.jsames.2010.04.002
1128 Starr, J.P., 1984. Geology and petrology of Rumiñahui volcano, Ecuador (Master's thesis).
1129 Departament of Geology of the University the Oregon, Oregon, USA.
1130 Steiger, R.H., Jäger, E., 1977. Subcommission on geochronology: Convention on the use of decay
1131 constants in geo- and cosmochronology. Earth and Planetary Science Letters 36, 359–362.
1132 https://doi.org/10.1016/0012-821X(77)90060-7
1133 Sun, S.-S., McDonough, W.F., 1989. Chemical and isotopic systematics of oceanic basalts:
1134 implications for mantle composition and processes. Geol. Soc. Lond. Spec. Publ. 42, 313–
1135 345. https://doi.org/10.1144/GSL.SP.1989.042.01.19
1136 Tsunematsu, K., Bonadonna, C., 2015. Grain-size features of two large eruptions from Cotopaxi
1137 volcano (Ecuador) and implications for the calculation of the total grain-size distribution. Bull
1138 Volcanol 77, 1–12. https://doi.org/10.1007/s00445-015-0949-4
1139 Vallejo, C., Almagor, S., Romero, C., Herrera, J.L., Escobar, V., Spikings, R., Winkler, W.,
1140 Vermeesch, P., 2020. Sedimentology, Provenance and Radiometric Dating of the Silante
1141 Formation: Implications for the Cenozoic Evolution of the Western Andes of Ecuador.
1142 Minerals 10, 929. https://doi.org/10.3390/min10100929
1143 Vallejo, C., Romero, C., Horton, B.K., Spikings, R.A., Gaibor, J., Winkler, W., Esteban, J.J.,
1144 Thomsen, T.B., Mariño, E., 2021. Jurassic to Early Paleogene sedimentation in the Amazon
1145 region of Ecuador: Implications for the paleogeographic evolution of northwestern South

America. Global and Planetary Change 204, 103555. https://doi.org/10.1016/j.gloplacha.2021.103555

Vallejo, C., Spikings, R., Horton, B.K., Luzieux, L., Romero, C., Winkler, W., Thomsen, T.B., 2019. Chapter 8 - Late cretaceous to miocene stratigraphy and provenance of the coastal forearc and Western Cordillera of Ecuador: Evidence for accretion of a single oceanic plateau fragment, in: Horton, B.K., Folguera, A. (Eds.), Andean Tectonics. Elsevier, pp. 209–236. https://doi.org/10.1016/B978-0-12-816009-1.00010-1

Vezzoli, L., Apuani, T., Corazzato, C., Uttini, A., 2017. Geological and geotechnical characterization of the debris avalanche and pyroclastic deposits of Cotopaxi Volcano (Ecuador). A contribute to instability-related hazard studies. Journal of Volcanology and Geothermal Research 332, 51–70. https://doi.org/10.1016/j.jvolgeores.2017.01.004

Winkler, W., Villagómez, D., Spikings, R., Abegglen, P., Tobler, St., Egüez, A., 2005. The Chota basin and its significance for the inception and tectonic setting of the inter-Andean depression in Ecuador. Journal of South American Earth Sciences, Cenozoic Andean Basin Evolution 19, 5–19. https://doi.org/10.1016/j.jsames.2004.06.006

Witt, C., Bourgois, J., 2010. Forearc basin formation in the tectonic wake of a collision-driven, coastwise migrating crustal block: The example of the North Andean block and the extensional Gulf of Guayaquil-Tumbes Basin (Ecuador-Peru border area). GSA Bulletin 122, 89–108. https://doi.org/10.1130/B26386.1

Witt, C., Bourgois, J., Michaud, F., Ordoñez, M., Jiménez, N., Sosson, M., 2006. Development of the Gulf of Guayaquil (Ecuador) during the Quaternary as an effect of the North Andean block tectonic escape. Tectonics 25. https://doi.org/10.1029/2004TC001723

Yamamoto, T., Kudo, T., Isizuka, O., 2018. Temporal variations in volumetric magma eruption rates of Quaternary volcanoes in Japan. Earth Planets Space 70, 1–12. https://doi.org/10.1186/s40623-018-0849-x

Yepes, H., Audin, L., Alvarado, A., Beauval, C., Aguilar, J., Font, Y., Cotton, F., 2016. A new view for the geodynamics of Ecuador: Implication in seismogenic source definition and seismic hazard assessment. Tectonics 35, 1249–1279. https://doi.org/10.1002/2015TC003941

Zernack, A.V., Procter, J.N., Cronin, S.J., 2009. Sedimentary signatures of cyclic growth and destruction of stratovolcanoes: A case study from Mt. Taranaki, New Zealand. Sedimentary Geology, Source to sink 220, 288–305. https://doi.org/10.1016/j.sedgeo.2009.04.024

Figure captions

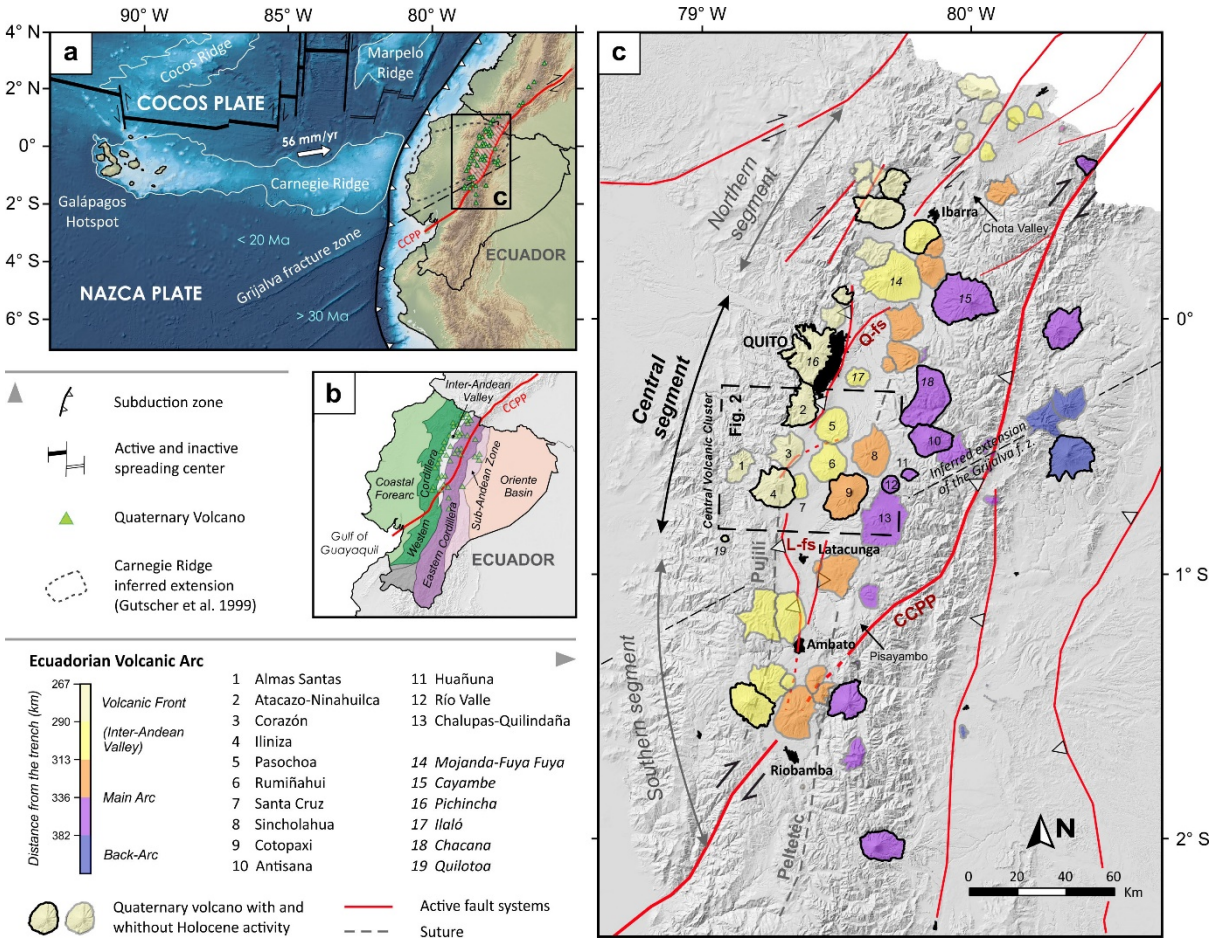

Figure 1. a) Regional geodynamic setting of the Ecuadorian margin. The white arrow indicates the direction of motion of the Nazca plate relative to South America (DeMets et al., 2010). Topography and bathymetry from the GEBCO 2020 program. **b)** Major geomorphologic provinces of Ecuador (modified from Litherland and Aspden, 1992). **c)** Schematic map of the Ecuadorian volcanic arc (modified from Bernard and Andrade, 2011). Volcanoes are colored according to their distance from the trench, which includes the N-S alignments of the Volcanic Front (Western Cordillera), Inter-Andean Valley, Main Arc (Eastern Cordillera), and Back-Arc. Variability in the number of volcanoes along-arc is represented by the northern, central, and southern across-arc segments. Active fault systems are represented by red lines according to Alvarado et al. (2016). CCPP: Chingual-Cosanga-Pallatanga-Puná Fault System; Q-fs: Quito Fault System; L-fs: Latacunga Fault System. Suture zones are shown by grey segmented lines. Major cities are shown in black.

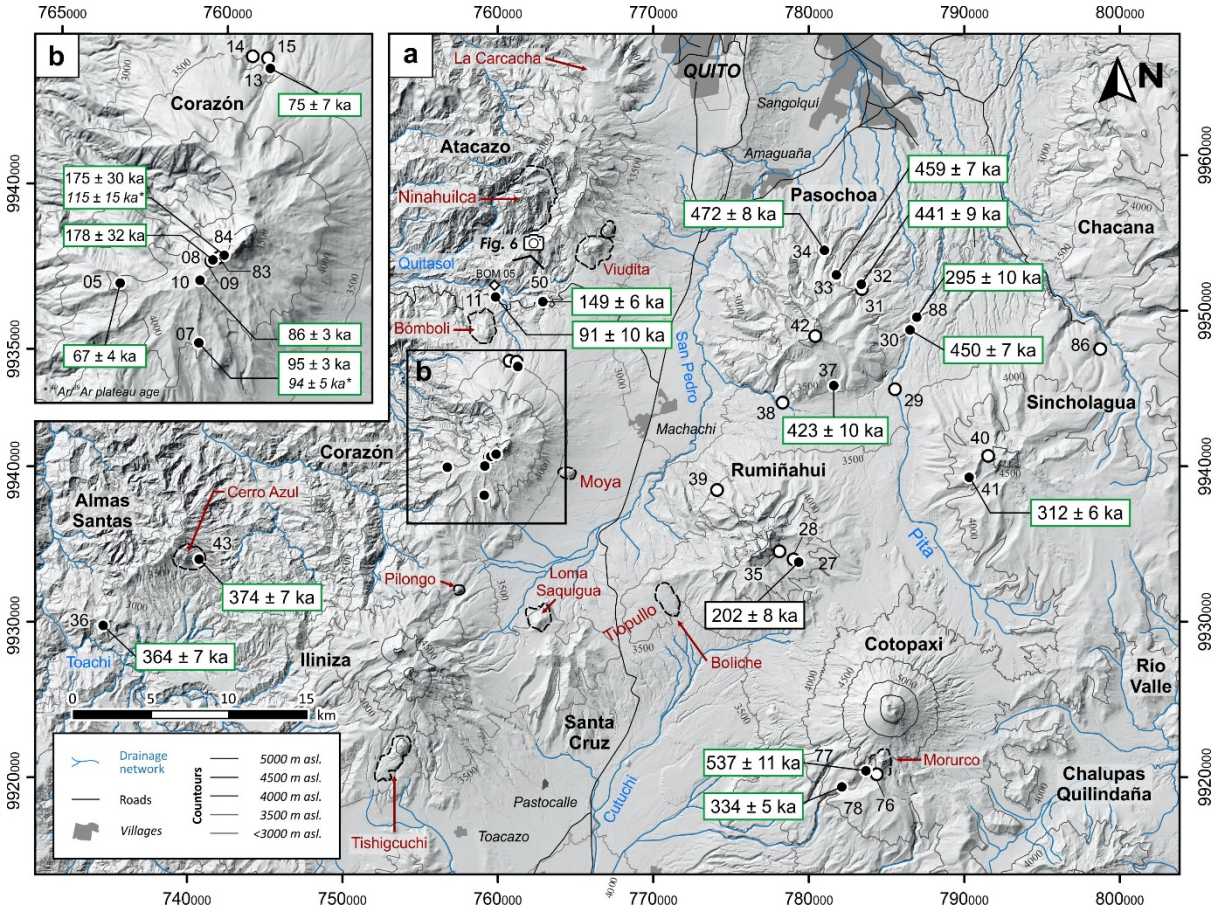

Figure 2. a) Hill-shaded digital surface model (from the Sigtierras program) of the central volcanic cluster of the Ecuadorian Arc showing the sampling locations and geochronological results. Numbers correspond to the last two digits of the sample's names (19EQxx or 20EQxx, depending on the year of recollection). K-Ar dated samples are shown as solid black dots. Volcanoes labelled in black. Satellite lava domes and cones are denoted by dashed lines and are labeled with red letters. Rivers and valleys names are labeled with blue letters. Coordinates are in Universal Transverse Mercator (UTM) zone 17. **b)** Extended view of the Corazón summit area. $^{40}Ar/^{39}Ar$ plateau ages are shown in italic letters.

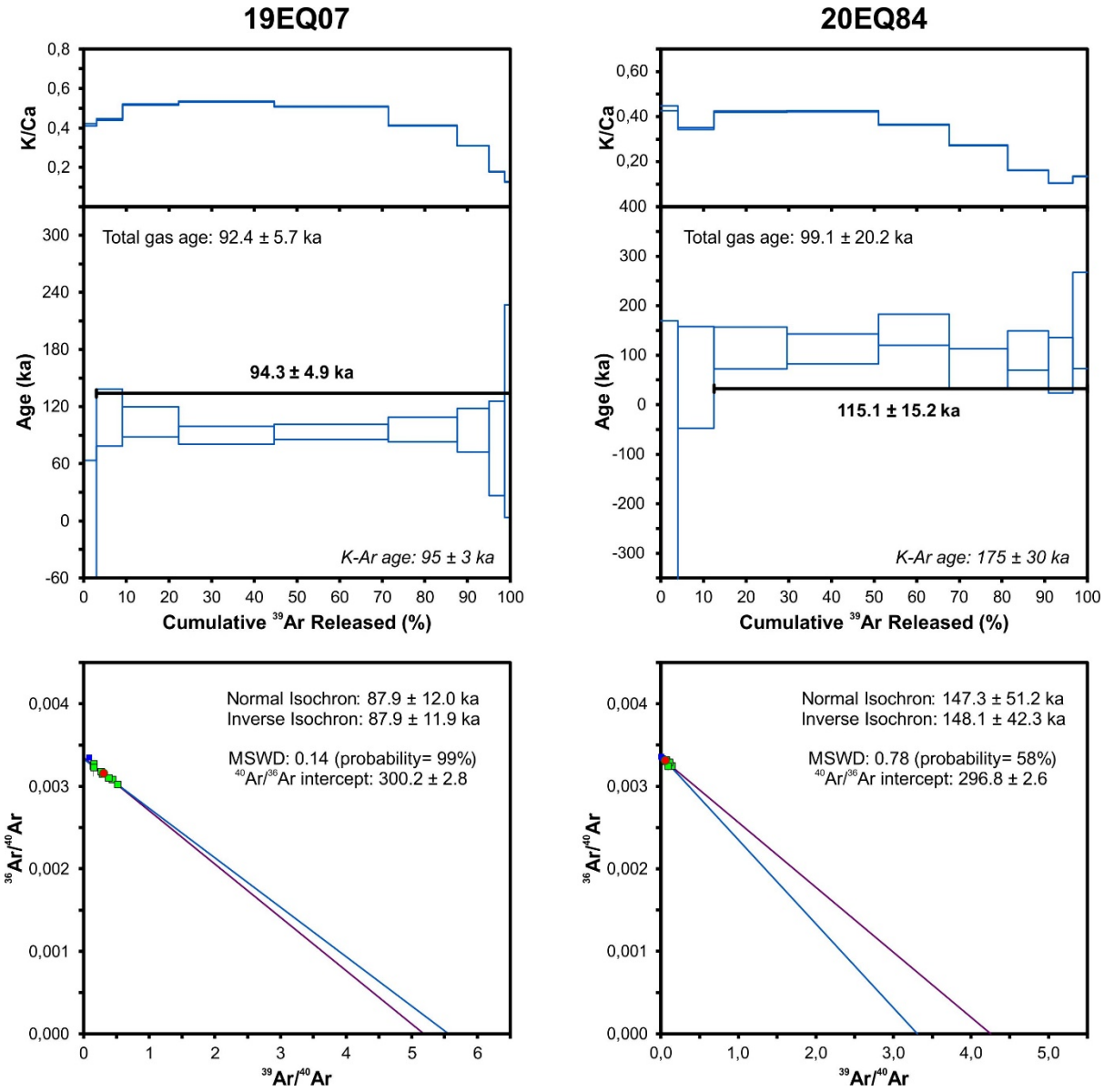

1202

1203 **Figure 3.** Results of $^{40}Ar/^{39}Ar$ analyses for samples 19EQ07 (left) and 20EQ84 (right). K/Ca ratio and
1204 apparent age spectra (in ka) are shown below as a function of the cumulative ^{39}Ar content (in %), inverse
1205 isochrons are shown below. Details are given in Appendix B.

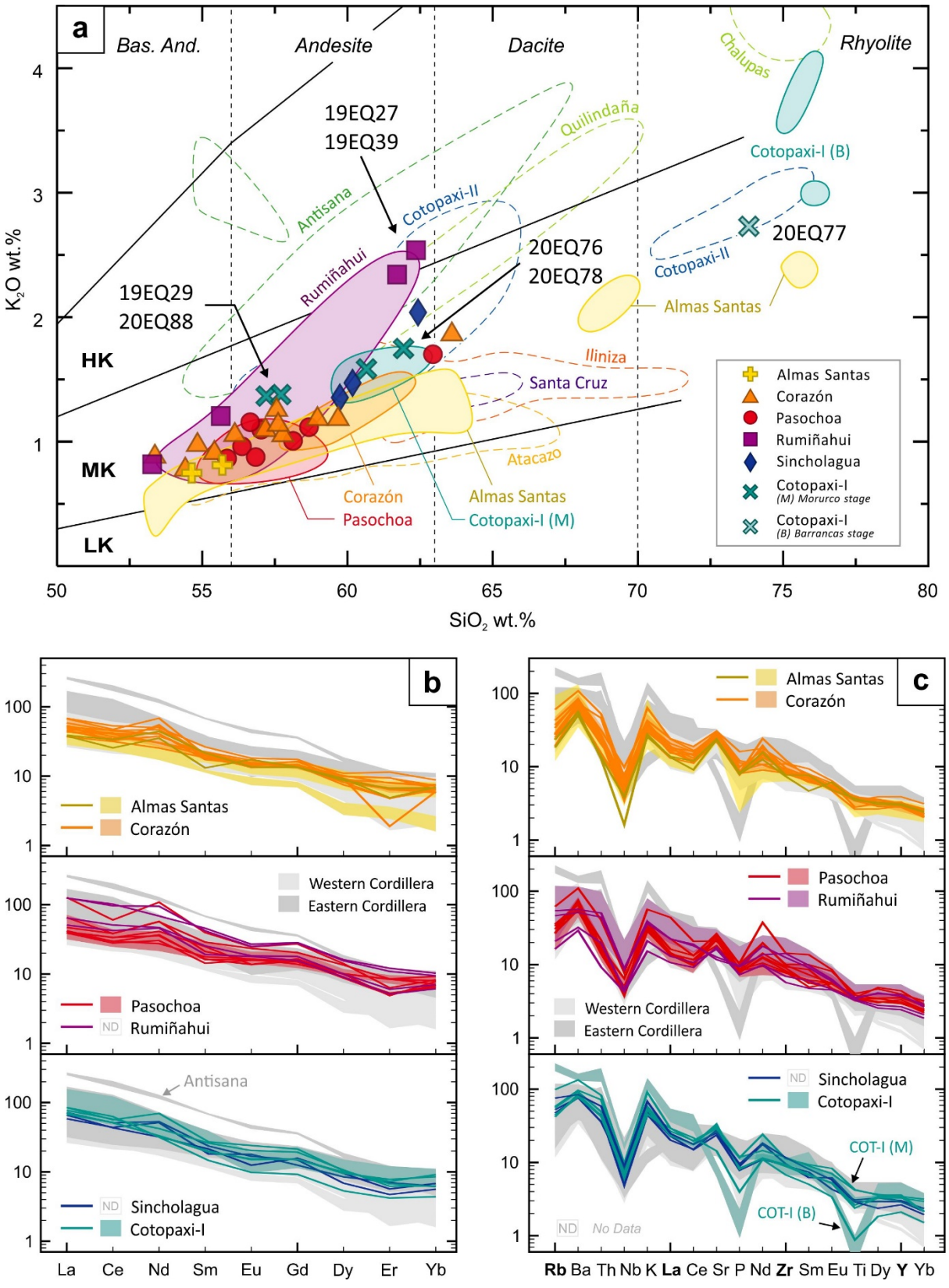

Figure 4. a) K_2O vs. SiO_2 diagram (Peccerillo and Taylor, 1976) for eruptive products of the central volcanic cluster. HK: high-K, MK: medium-K, and LK: low-K calc-alkaline series. Data from this study represented as point symbols. Shaded areas represent the compositional fields of volcanoes sampled in

this study while dashed areas are for other volcanoes, both areas with data taken from the Georoc database and other studies (Starr, 1984; Chemin, 2004; Garrison et al., 2006; Bellot-Gurlet et al., 2008; Schiano et al., 2010; Ancellin et al., 2017; Hall et al., 2017b; Bablon et al., 2020b; Chiaradia et al., 2020; Córdova et al., 2020; Santamaría et al., 2022). **b)** Rare Earth Elements normalized to chondrites, and **c)** Incompatible trace elements normalized to the primitive mantle diagrams (Sun and McDonough, 1989) for the same arrangements. The sampled volcanoes were organized according to their location in the Western Cordillera (yellow and orange lines), the Inter-Andean Valley (red and purple lines), and the Eastern Cordillera (blue and turquoise lines). The shaded areas represent the compositional fields from bibliographic data; volcanoes with insufficient data are denoted as ND fields.

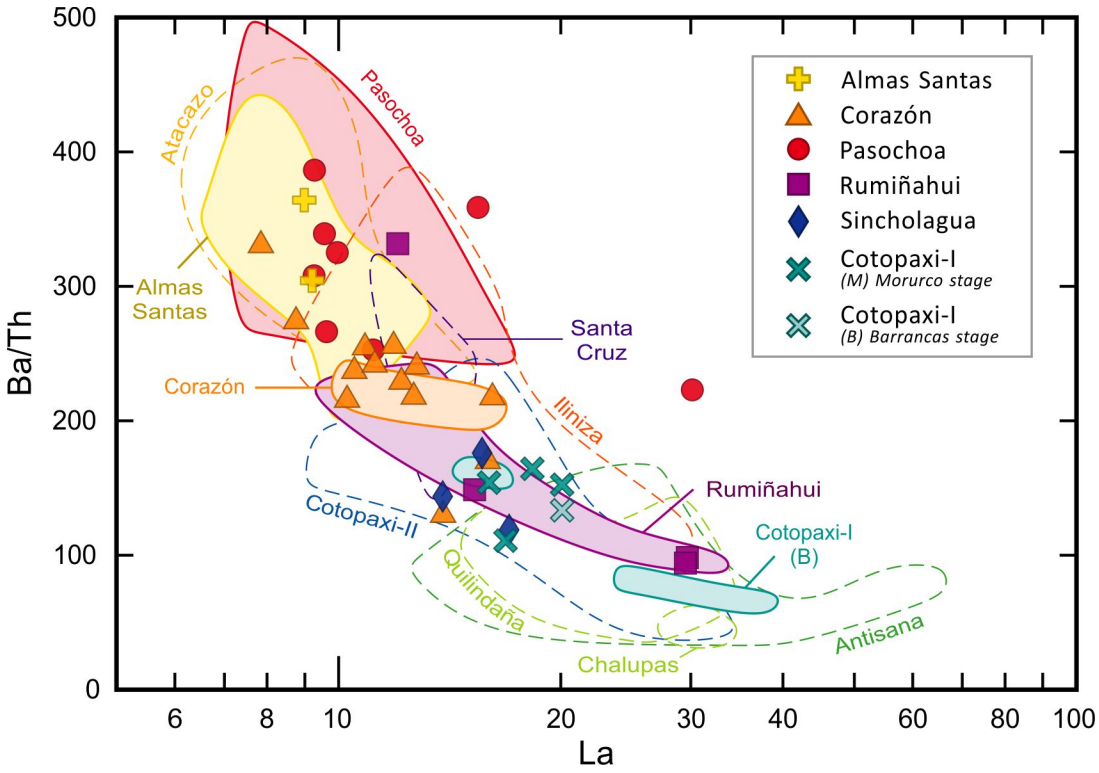

Figure 5. Ba/Th vs La diagram for eruptive products of the central volcanic cluster. Same data as Fig. 4a. Data from this study represented as point symbols. Shaded areas represent the compositional fields of volcanoes sampled in this study while dashed areas are for other volcanoes, both areas with data taken from the Georoc database and other studies (Starr, 1984; Chemin, 2004; Garrison et al., 2006; Bellot-Gurlet et al., 2008; Schiano et al., 2010; Ancellin et al., 2017; Hall et al., 2017b; Bablon et al., 2020b; Chiaradia et al., 2020; Córdova et al., 2020; Santamaría et al., 2022)

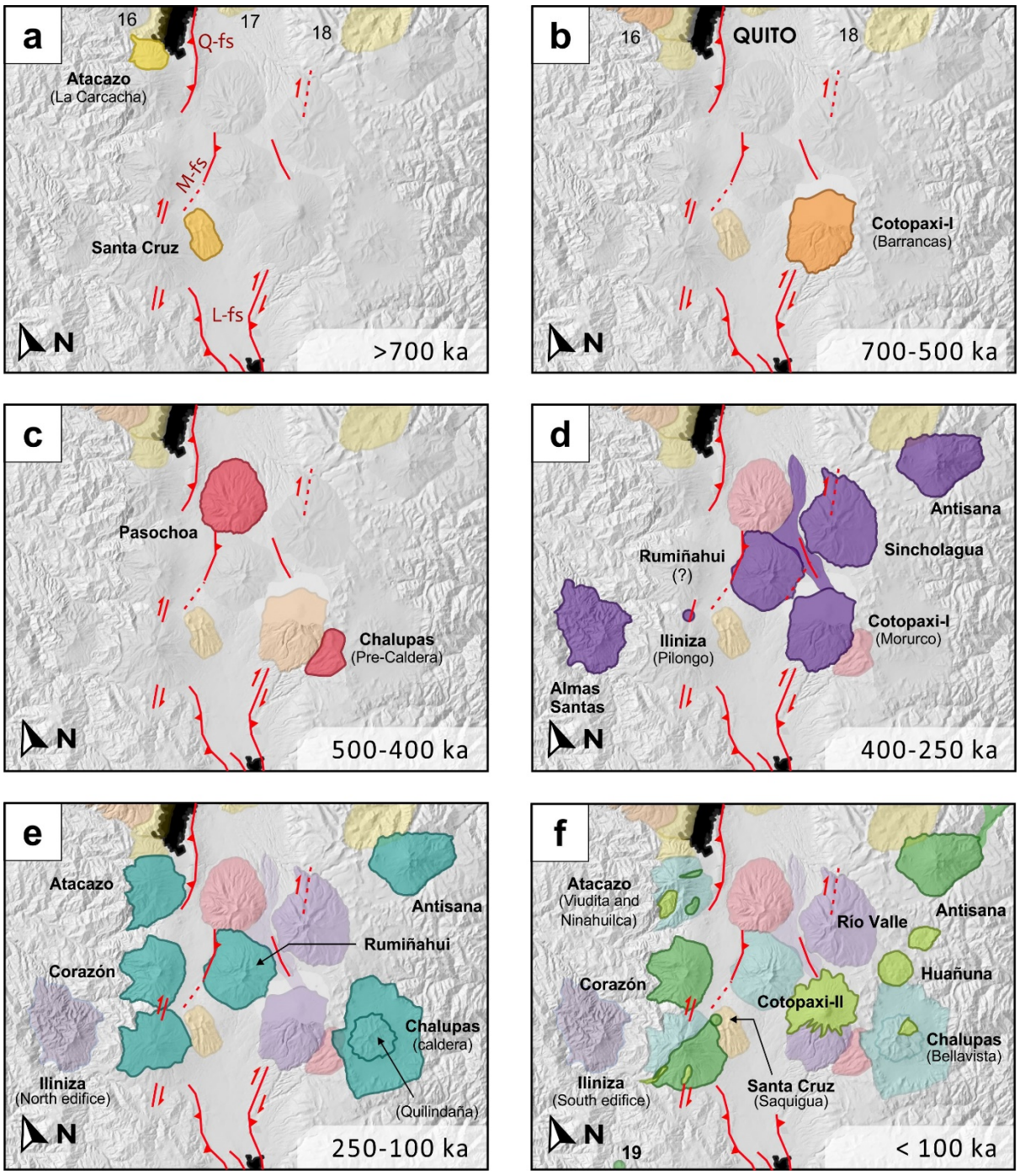

Figure 6. Synthesis cartoons of the eruptive history of the Ecuadorian central arc segment. **a)** Early stage of the Quaternary volcanic arc. Formation of the volcanoes Carcacha (1.3 Ma) and Santa Cruz (700 ka), as well as other contemporaneous edifices outside the study area: El Cinto (16), Ilaló (17), Chacana (18). **b)** Early construction of the volcanic cluster. Cotopaxi-I (Barrancas stage) at 550 ka. **c)** Pasochoa; Chalupas (pre-caldera deposits). **d)** Antisana-I; Almas Santas; Cotopaxi-I (Morurco stage); Pilongo lava dome of Iliniza; early stage of Rumiñahui; and Sincholagua. The distal flows of the Morurco cone are represented as a purple field north of Cotopaxi-I. **e)** Antisana; Atacazo; Chalupas caldera-forming eruption (216 ± 5 ka; Bablon et al., 2020b), and construction of the Quilindaña post-

caldera edifice; Corazón; North Iliniza edifice; late stage of Rumiñahui. **f)** Modern stage of the volcanic cluster (dark green) and its Holocene activity (light green). Antisana II and III; Atacazo satellite lava domes, and Ninahuilca lava dome complex; Corazón; Cotopaxi-II edifice; Bellavista lava dome; Huañuna lava dome; South Iliniza edifice, and its satellite lavas; Rio Valle lava dome; and Quilotoa caldera (19). Active fault systems are shown as red lines for all charts, according to Alvarado et al. (2016) and this study. Note that the maps are rotated slightly counterclockwise to match with the E-W orientation of the volcanic cluster. See text for full references.

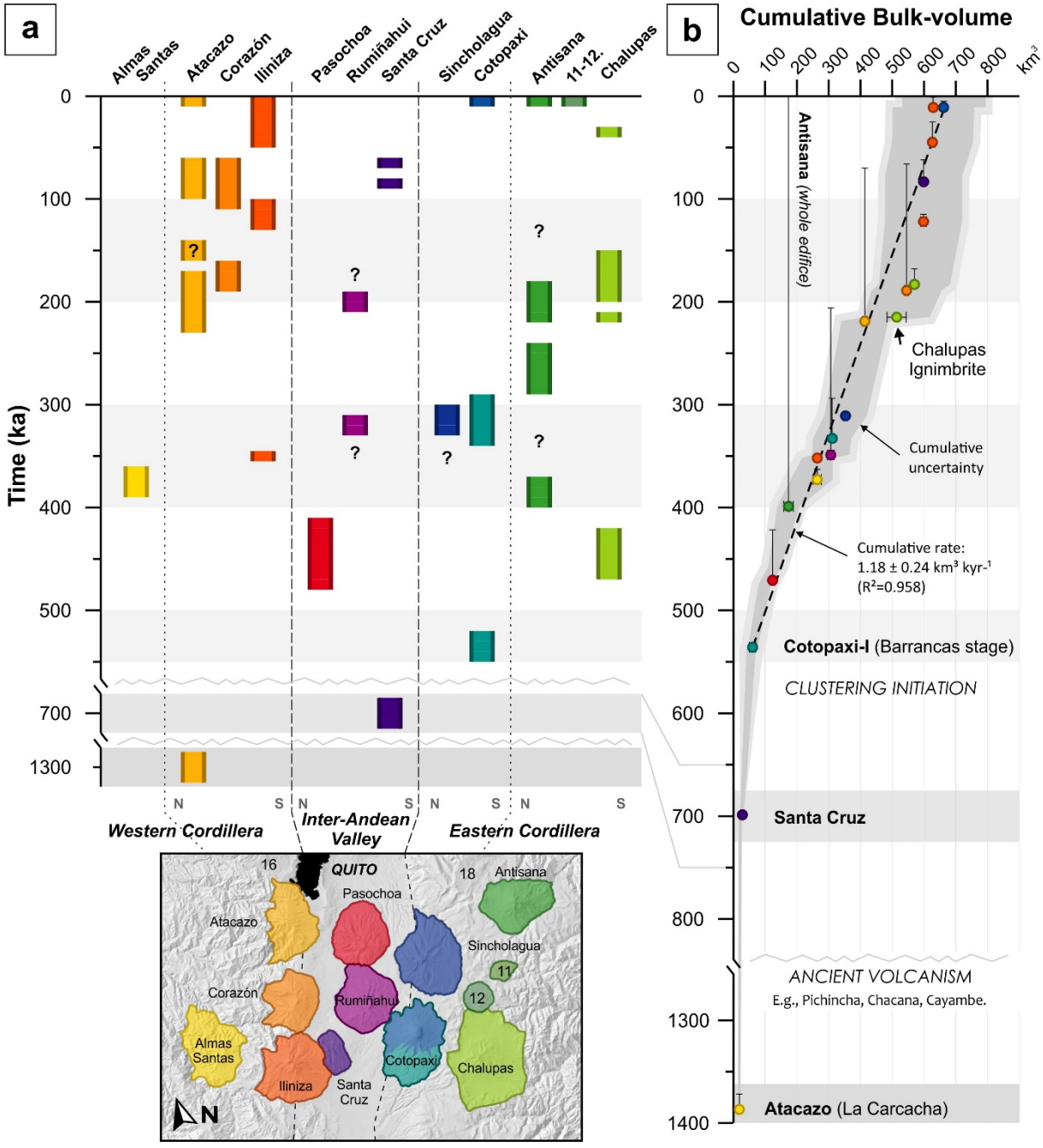

Figure 7. Temporal evolution of volcanism in the central segment of the Ecuadorian Arc**. a)** Schematic representation of the individual cone-building stages through time. See text for details. **b)** Cumulative bulk volume (km^3) for the central volcanic cluster over time. Uncertainty bars indicate the extent of the considered construction periods in ka according to Table 2. The bulk volumes of Antisana, Rumiñahui, Corazón and Atacazo volcanoes do not distinguish the different cone-building stages due to the lack of detailed stratigraphic data. The dashed line symbolizes the cumulative volume rate over the last ~550 ka, while the shaded area represents the cumulative volumetric uncertainty range. Volcano numbers as in Figure 1.

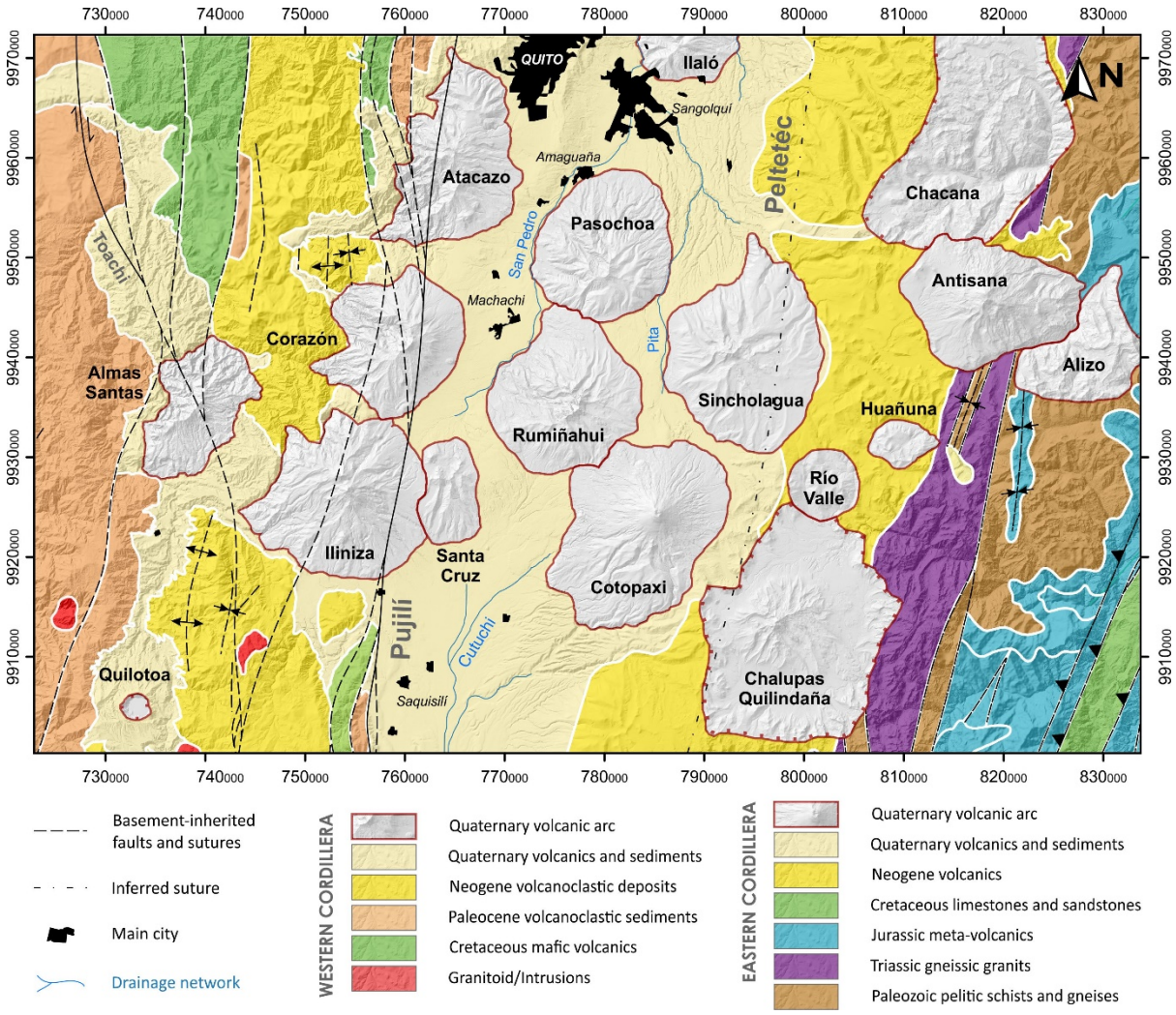

Figure 8. Geologic map of the central segment basement (modified from Litherland et al., 1994; Hughes and Bermúdez, 1997; Egüez et al., 2017; Vallejo et al., 2020). Dashed lines show tectonic structures inherited from the basement. The Pujilí suture is drawn as a continuous line, and the inferred location of the Peltetec suture as a dotted line.

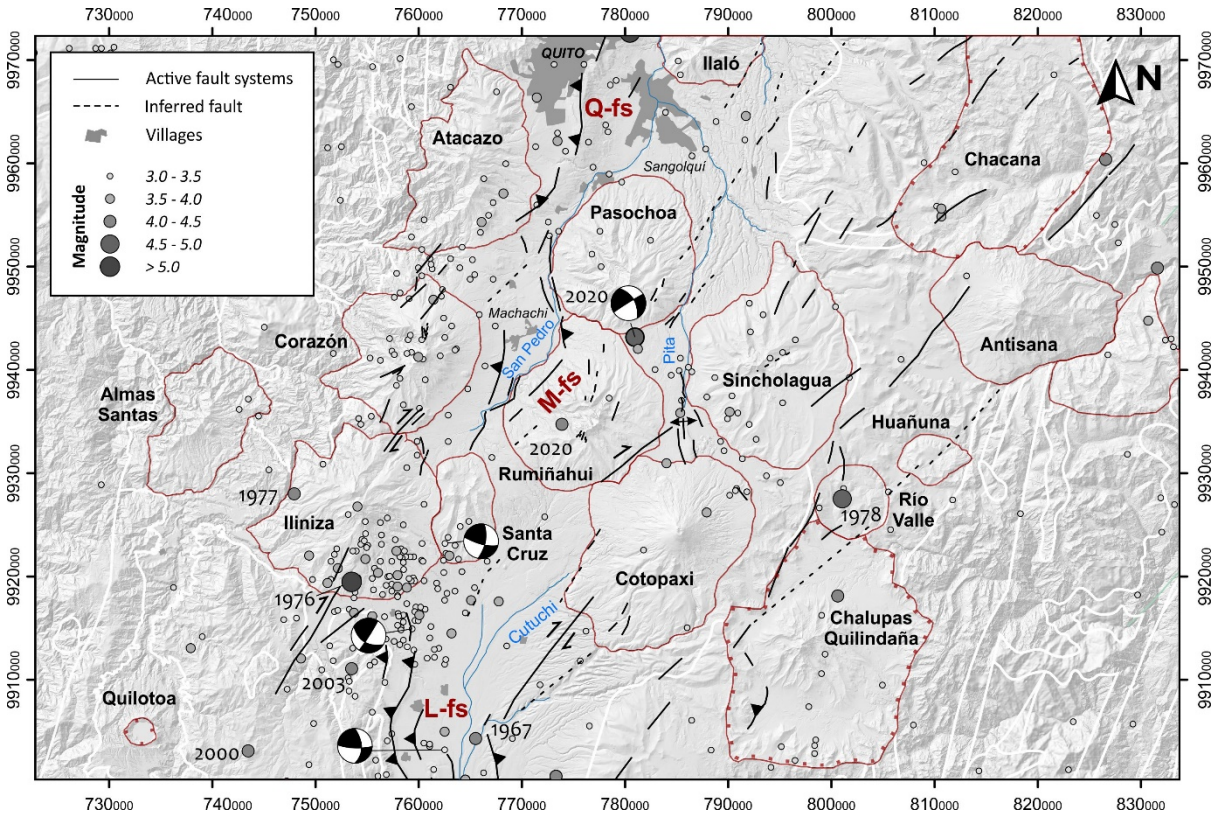

Figure 9. Schematic map of the Quaternary fault systems of the central segment focused in the Inter-Andean Valley (Egüez and Yepes, 1994; Alvarado, 2012; Alvarado et al., 2014; Fiorini and Tibaldi, 2012; and this study). Q-fs: Quito fault-system; L-fs: Latacunga fault-system; M-fs: Machachi fault-system. Locations of the historical earthquakes according to the "Catalogo Homogenizado 1587 – 2011" of the IG-EPN, with hypocenter depths less than 40 km. The location of the AD 2020 earthquake according to Hernández et al. (2020). Moment tensor solutions from Basualto and Troncoso (2003) and Hernández et al. (2020).

Tables

Table 1. K-Ar ages obtained in this study for central segment volcanoes. Column headings indicate sample name, outcrop nature and relative location, sample coordinates projected using the Universal Transverse Mercator (UTM) coordinate system (Zone 17), potassium (K) content in percent, radiogenic argon (^{40}Ar*) content in percent and in 10^{11} atoms per gram, age obtained for each measurement, and weighted mean age in ka given with a 1-σ uncertainty. All measurements were performed on groundmass, except for one sample measured on plagioclase phenocrysts (^{P}) and one sample measured on volcanic glass (^{G}).

Sample	Location and Unit	UTM Easting	UTM Northing	K (%)	^{40}Ar* (%)	^{40}Ar* (10^{11} at/g)	Age ± 1 σ (ka)	Mean age (ka)
Almas Santas volcano								
19EQ43	Lava flow, Cerro Azul	740786	9934033	0.992	8.4%	3.8562	372 ± 7	**374 ± 7**
					8.1%	3.8998	377 ± 7	
19EQ36	Lava flow, Tangan	734605	9929768	0.756	8.2%	2.8759	364 ± 7	**364 ± 7**
					7.4%	2.8822	365 ± 7	
Corazón volcano								
19EQ08	Lava flow, pyramidal peak	759536	9940634	1.579	0.6%	2.9028	176 ± 28	**178 ± 32**
					0.5%	2.9836	181 ± 38	
20EQ84	Lava flow, pyramidal peak	759883	9940775	0.972	0.6%	1.7824	176 ± 30	**175 ± 30**
					0.6%	1.7798	175 ± 29	
19EQ07	Lava flow, S flank	759112	9938136	1.334	3.9%	1.3350	96 ± 3	**95 ± 3**
					3.6%	1.2996	93 ± 3	
19EQ11	Lava flow, Cerro Bómboli	759847	9950892	1.323	0.9%	1.2223	88 ± 10	**91 ± 10**
					1.0%	1.3013	94 ± 10	
19EQ10	Lava flow, S flank	759148	9940026	1.057	2.8%	0.9700	88 ± 3	**86 ± 3**
					2.7%	0.9196	83 ± 3	
19EQ13	Lava flow, N flank	761280	9946424	1.279	1.1%	1.0225	77 ± 7	**75 ± 7**
					1.1%	0.9799	73 ± 6	
19EQ05	Lava flow, SW flank	756746	9939943	0.966	2.0%	0.7031	70 ± 4	**67 ± 4**
					1.9%	0.6539	65 ± 4	
Atacazo volcano								
20EQ50	Dacite block, S avalanche	762881	9950592	1.279	2.5%	1.9833	148 ± 6	**149 ± 6**
					2.8%	2.0019	150 ± 6	

Sample	Location and Unit	UTM Easting	UTM Northing	K (%)	^{40}Ar* (%)	^{40}Ar* (10^{11} at/g)	Age ± 1 σ (ka)	Mean age (ka)
Pasochoa volcano								
19EQ34	Lava flow, N flank	780987	9953901	0.856	12.0%	4.1969	469 ± 8	**472 ± 8**
					12.4%	4.2349	474 ± 8	
19EQ33	Lava flow, N flank	781758	9952313	1.807	26.5%	8.6492	458 ± 7	**459 ± 7**
					28.9%	8.6627	459 ± 7	
19EQ30	Lava flow, E flank	786494	9948763	1.080	11.5%	5.1295	455 ± 8	**450 ± 7**
					13.3%	5.0254	446 ± 7	
19EQ32	Lava flow, NW flank	783362	9951701	1.093	6.9%	5.0002	438 ± 9	**441 ± 9**
					7.1%	5.0665	444 ± 9	
19EQ37	Lava flow, S flank	781599	9945191	1.086	5.2%	4.7482	419 ± 10	**423 ± 10**
					5.1%	4.8376	427 ± 10	
Rumiñahui volcano								
19EQ27 [P]	Lava flow, E flank	779336	9933840	0.523	47.7%	1.0812	198 ± 8	**202 ± 8**
					43.4%	1.1254	206 ± 8	
Sincholagua volcano								
19EQ41	Lava flow, summit area	790298	9939301	1.739	9.0%	5.6975	314 ± 6	**312 ± 6**
					9.2%	5.6261	310 ± 6	
Cotopaxi volcano								
20EQ77 [G]	Obsidian flow, Morurco peak base	783660	9920417	2.430	6.2%	13.5144	532 ± 11	**537 ± 11**
					6.4%	13.7703	542 ± 11	
20EQ78	Lava flow, Morurco peak	782119	9919377	1.743	13.0%	6.1003	335 ± 5	**334 ± 5**
					12.7%	6.0550	333 ± 5	
20EQ88	Lava flow, Tanipamba (Pita valley)	786939	9949596	1.746	3.0%	5.3977	296 ± 11	**295 ± 10**
					3.9%	5.3573	294 ± 9	

1276

1277 **Table 2.** Construction and erosion volumes calculated from numerical reconstructions. Results
1278 are given with a 1-σ uncertainty (see text for details).

Volcano	Construction Volume (km^3)	Uncertainty percentage	Present-day Volume (km^3)	Erosion Volume (km^3)	Erosion percentage	Reference
Almas Santas	90 ± 14	15%	25 ± 10	67 ± 3	74%	This study
Atacazo	61 ± 7	12%	25 ± 6	36 ± 1	60%	This study
Carcacha	8 ± 1	12%	5 ± 1	3 ± 0	41%	This study
Corazón	31 ± 7	21%	9 ± 7	22 ± 0	71%	This study
Pasochoa	63 ± 6	10%	44 ± 5	19 ± 1	30%	This study
Rumiñahui	43 ± 10	24%	22 ± 10	21 ± 1	49%	This study
Santa Cruz	21 ± 3	15%	~16	~5	24%	This study
Sincholagua	42 ± 7	16%	11 ± 5	31 ± 2	74%	This study
Cotopaxi II	32 ± 3	9%	29 ± 3			This study
Quilindaña	25 ± 3	18%	9 ± 1	16 ± 1	63%	This study
North Iliniza	28 ± 9	32%	~22	6 ± 2	21%	Santamaría et al. (2022)
South Iliniza	18 ± 6	33%	~12	6 ± 2	33%	Santamaría et al. (2022)
Iliniza (whole)	46 ± 15	32%	34 ± 14	12 ± 4	26%	Santamaría et al. (2022)
Cotopaxi I – Barrancas stage	~32					Hall and Mothes (2008)
Cotopaxi I – Morurco stage	~4					Hall and Mothes (2008)
Cotopaxi II	~51					Hall and Mothes (2008)
Antisana (whole)	~50					Hall et al. (2017b)
Chalupas (bulk)	230 ± 30	8%				Bablon et al. (2020b)
Chalupas (DRE)	~100					Hall and Mothes (2008) Crosweller et al. (2012)

1279
1280

1281 **Table 3.** Generalized chronostratigraphy of the central volcanic cluster of the Ecuadorian arc
1282 showing the main cone-building stages of its volcanoes

Volcano	NW-SE Aligment	Location	Cone-building stage	Magma Composition	Age (ka)	References
Ancient volcanism	All	North of lat. 0°20'S	E.g., Pichincha (El Cinto), Chacana (old lavas), Cayambe (Viejo Cayambe)		>1 Ma	Samaniego et al., (2005); Opdyke et al., (2006); Robin et al., (2010); Bablon et al., (2020a)
Almas Santas	Volcanic Front	lat. 0°35'S long. 78°51'W	Early stage (andesite lavas)	53-57 wt.% SiO_2 medium-K series	~375 to ~365	Chemin, (2004); This study
			Late stage and Cerro Azul satelite lavas	57-63 and 67-75 wt.% SiO_2 medium-K series	< 365 ka	Chemin, (2004); This study
Atacazo-Ninahuilca	Volcanic Front	lat. 0°19'S long. 78°36'W	La Carcacha edifice	60-61 wt.% SiO_2 medium-K series	~1.3 Ma	Hidalgo, (2006)
		lat. 0°21'S long. 78°37'W	Atacazo edifice and satellite lava domes	57-63 and 66-67 wt.% SiO_2 medium-K series	~200 to ~71 ka	Hidalgo, (2006); This study
		lat. 0°23'S long. 78°39'W	Ninahuilca dome complex	61-66 wt.% SiO_2 medium-K series	<8 ka	Hidalgo, (2006)
Corazón	Volcanic Front	lat. 0°32'S long. 78°40'W	Main Edifice	53-64 wt.% SiO_2 medium-K series	~115 to ~70 ka	Chiaradia et al., (2009); This study
Iliniza	Volcanic Front	lat. 0°37'S long. 78°41'W	Pilonga lava dome	68-69 wt.% SiO_2 medium-K series	353 ± 6 ka	Hidalgo et al., (2007); Santamaría et al., (2022)
		lat. 0°39'S long. 78°43'W	North Iliniza edifice	62-65 wt.% SiO_2 medium-K series	~125 to ~115 ka	Hidalgo et al., (2007); Santamaría et al., (2022)
		lat. 0°40'S long. 78°43'W	South Iliniza edifice and late satellite lavas	59-72 and 59-63 wt.% SiO_2 medium-K series	~45 to ~6 ka	Hidalgo et al., (2007); Santamaría et al., (2022)
Pasochoa	Inter-Andean Valley	lat. 0°28'S long. 78°29'W	Main Edifice	55-61 wt.% SiO_2 medium-K series	~470 to ~425 ka	Schiano et al., (2010); This study
Rumiñahui	Inter-Andean Valley	lat. 0°35'S long. 78°30'W	Early stage	53-58 wt.% SiO_2 medium-K series	>300 ka	Starr, (1984); This study
			Late stage	61-63 wt.% SiO_2 high-K series	~210 ka	Starr, (1984); This study
Santa Cruz	Inter-Andean Valley	lat. 0°39'S long. 78°38'W	Main Edifice	56-66 wt.% SiO_2 medium-K series	~700 ka	Santamaría et al., (2022)
			Loma Saquigua cone	58-64 wt.% SiO_2 medium-K series	~80 to ~60 ka	Santamaría et al., (2022)
Sincholagua	Main arc	lat. 0°32'S long. 78°22'W	Main Edifice	59-61 wt.% SiO_2 medium-K series	~310 ka	This study
Cotopaxi	Main arc	lat. 0°43'S long. 78°27'W	Barrancas stage	74-77 wt.% SiO_2 medium- to high-K series	~540 ka	Hall and Mothes, (2008); Garrison et al., (2011); This study
			Morurco stage	57-63 wt.% SiO_2 medium-K series	~335 to ~295 ka	Hall and Mothes, (2008); Garrison et al., (2011); This study
		lat. 0°41'S long. 78°26'W	Cotopaxi II	56-66 and 70-76 wt.% SiO_2 medium- to high-K series	<13 ka	Hall and Mothes, (2008); Garrison et al., (2011)
Antisana	Main arc	lat. 0°29'S long. 78°08'W	Main Edifice	54-68 wt.% SiO_2 medium- to high-K series	~400 to <0.8 ka	Hall et al., (2017b)
			Cuyuja lava flow	55-58 wt.% SiO_2 high-K andesite series	210 ± 30 ka	Hall et al., (2017b)
Huañuna	Main arc	lat. 0°37'S long. 78°14'W	Lava dome	Rhyolitic lavas high-K series	~12 and ~10 ka	Mothes and Hall, (2008); Hall et al., (2017b)
Chaupiloma (Rio Valle)	Main arc	lat. 0°40'S long. 78°16'W	Lava dome	Rhyolitic lavas high-K series	~15 to 6 ka	Mothes and Hall, (2008); Hall et al., (2017b)
Chalupas-Quilindaña	Main arc	lat. 0°48'S long. 78°23'W	Pre-caldera lavas	55-71 wt.% SiO_2 high-K series	~460 to ~420 ka	Hammersley, (2003); Córdova et al., (2020)

	lat. 0°47'S long. 78°20'W	Caldera-forming ignimbrite eruption	73-76 wt.% SiO_2 high-K series	216 ± 5 ka	Hammersley, (2003); Bablón et al., (2020b); Córdova et al., (2020)
	lat. 0°47'S long. 78°20'W	Quilindaña	57-70 wt.% SiO_2 high-K series	~185 to ~45 ka	Hammersley, (2003); Córdova et al., (2020)

1283

1284